Orr mechanism in transition of parallel shear flow

Yuxin Jiao,[*] Yongyun Hwang,[†] and Sergei I. Chernyshenko[‡]
Department of Aeronautics, Imperial College, London SW7 2AZ, United Kingdom

(Received 4 August 2020; accepted 15 January 2021; published 5 February 2021)

The Orr mechanism is revisited to understand its precise role in the transition of plane Couette flow. By considering homogeneous shear flow and plane Couette flow, it is identified that the Orr mechanism induces a lift-up effect which significantly amplifies spanwise velocity. An optimal perturbation analysis for an individual velocity component reveals that the amplification of spanwise velocity is most active at the streamwise length comparable to the given spanwise length of the perturbation. The relevance of this mechanism to transition is subsequently examined in plane Couette flow. To this end, a set of initial conditions, which combines the optimal perturbation for spanwise velocity with the one for all the velocity components, is considered by varying their amplitudes. Two representative transition scenarios are found: oblique and streak transitions. In the former, the spanwise velocity perturbation amplified with the Orr mechanism initiates both streak amplification and breakdown, whereas in the latter, its role is limited only to the streak breakdown at the late stage of transition. As such, the oblique transition offers a route to turbulence energetically more efficient than the streak transition, at least for the cases examined in the present paper. Finally, the oblique transition is found to share many physical similarities with the transition by the minimal seed.

DOI: 10.1103/PhysRevFluids.6.023902

I. INTRODUCTION

It has been well understood that a small-amplitude perturbation to a linearly stable laminar base flow can experience a transient growth as a result of the non-normality of the linearized Navier-Stokes operator [1–3]. One of the well-known physical mechanisms for the transient growth is the "lift-up" effect, by which streamwise vortices are converted into streaks with a large amplification of energy from base/mean flow [4–6]. The initial condition, which leads to the largest transient energy growth, has often been referred to as "optimal perturbation," and it has extensively been computed in most of the canonical laminar shear flows [2,3,7,8]. The emergence of streaks has been observed as a robust feature in transitions taking place in the absence of Tollmien-Schilichting waves [9–16]. Furthermore, the lift-up effect has also been understood as the key mechanism of the generation of streaks in turbulent flows [17–24].

Another well-known mechanism of transient energy growth is the Orr mechanism. It was originally proposed by Orr [25], who demonstrated that the perturbation energy of a given velocity field can grow transiently in time, as the perturbation field, initially inclined towards the upstream, is gradually tilted downstream by base/mean shear. The Orr mechanism was also observed in the early transient-growth studies of two-dimensional perturbation in shear flow [26,27]. However, despite

[*]y.jiao17@imperial.ac.uk
[†]y.hwang@imperial.ac.uk
[‡]s.chernyshenko@imperial.ac.uk

the well-established mathematical description of the Orr mechanism, its precise physical role in the transition to turbulence remains unclear. A well-studied scenario of the bypass transition, which we shall refer to as a "streak transition," is typically described as (e.g., Ref. [27]) (1) the linear growth of streaks from a streamwise vortical perturbation via lift-up effect [2,3,7,8], or (2) a secondary instability or transient growth of amplified streaks and a subsequent nonlinear breakdown leading to turbulence [28–33]. In this scenario, a possible role played by the Orr mechanism may lie in the evolution of the perturbation for secondary transient growth [30], as this would be a mechanism for the generation of a spanwise velocity perturbation leading to a strong interaction with the least stable streak instability modes (sinuous modes, in particular) [31,33].

Recently, an optimal initial condition, which takes the nonlinearity of the Navier-Stokes equations fully into account, has been computed for the transition to turbulence in canonical wall-bounded shear flows [34–38] (see Ref. [39] for a review on this issue). The initial condition, often referred to as the "minimal seed" for the transition to turbulence, is designed to trigger turbulence by reaching the laminar-turbulence separatrix (i.e., the "edge" of turbulence [40,41]) with the lowest perturbation energy. The minimal seed typically emerges as a highly localized three-dimensional structure in space. In the earliest stage of its evolution, the localized initial perturbation is amplified via the Orr mechanism, and is subsequently converted into a streamwise elongated streak via the lift-up effect. The streamwise meandering motion of the streak, which highly resembles the sinuous mode of streak instability, ensues rapidly, resulting in a nonlinear breakdown to form a localized turbulence (or turbulence spot). Finally, the turbulence spot gradually spreads over the space, eventually evolving into fully developed turbulence.

In the two transition scenarios described above, there is an important difference in the roles played by the Orr mechanism. In the former case, the Orr mechanism may primarily be active in the secondary instability and/or transient growth process to facilitate the generation of spanwise velocity perturbation. On the contrary, in the latter case, the Orr mechanism emerges at the earliest stage of transition where a streak is not even developed in the flow. Given that the latter transition scenario is the most energetically efficient route to turbulence, this suggests that the activation of the Orr mechanism at an appropriate stage of transition may be the key physical element to trigger turbulence with a small amount of initial perturbation energy.

The purpose of this paper is to explore the possible roles played by the Orr mechanism in the transition of parallel shear flows. We first revisit the linear amplification process in homogeneous shear flow. Particular attention of the analysis will be paid to the precise understanding of the Orr mechanism and the resulting growth mechanism. Indeed, we shall see that the Orr mechanism induces a lift-up effect, which subsequently amplifies both streamwise and spanwise velocities. Computation of optimal perturbation for an individual velocity component reveals that this mechanism leads to the largest amplification of spanwise velocity at a streamwise wavelength comparable to the given spanwise wavelength. The optimal perturbation for the spanwise velocity is then utilized to examine the transition scenarios mediated by the Orr mechanism in plane Couette flow. In particular, by introducing a set of initial conditions suitably combining the linear optimal perturbation for spanwise velocity with the one for all the velocity components, two energetically efficient routes of transition have been identified, consistent with previous studies: (1) an oblique transition [42,43], and (2) a streak transition [33]. It is found that the oblique transition [42,43] is initiated by the Orr mechanism and that the resulting spanwise velocity perturbation promotes the early-stage streak development as well as its breakdown at the late stage of transition. On the contrary, in the streak transition, the role of the Orr mechanism is limited to the generation of a spanwise velocity perturbation to promote streak breakdown at the late stage. As such, the oblique transition is found to offer a more energetically efficient route to turbulence than the streak transition, while sharing many physical similarities with the transition by the minimal seed.

II. THE ORR MECHANISM REVISITED

A. Homogeneous shear flow

For the purpose of revisiting the role of the Orr mechanism in the context of linear stability, we first consider a unbounded homogeneous shear flow of incompressible fluid with density ρ and kinematic viscosity ν. The linearized equations of motion in this flow admit the unique analytical solution, allowing for an in-depth discussion on the Orr mechanism and the resulting physical processes. The flow variables are made dimensionless with a characteristic velocity $\mathcal{U}$ and length $\mathcal{L}$, which will be defined later. We denote by x_1, x_2, and x_3 the dimensionless streamwise (x), vertical (y), and spanwise (z) coordinates, respectively. The dimensionless momentum equations of motion in the perturbation forming about the base flow $\mathbf{U}$ [$=(y, 0, 0)$] are given by

$$\frac{\partial \mathbf{u}}{\partial t} + (\mathbf{U}\cdot\nabla)\mathbf{u} + (\mathbf{u}\cdot\nabla)\mathbf{U} = -\nabla p + \frac{1}{\mathrm{Re}}\nabla^2\mathbf{u} + \mathbf{N}(\mathbf{u}), \tag{1}$$

where t is the dimensionless time, $\mathbf{u} = (u, v, w)$ the perturbation velocity, which will be interchangeably used with $\mathbf{u} = (u_1, u_2, u_3)$, p the perturbation pressure, $\mathbf{N}(\mathbf{u}) = -(\mathbf{u}\cdot\nabla)\mathbf{u}$, and Re ($\equiv \mathcal{U}\mathcal{L}/\nu$) the Reynolds number.

The linearized version of Eq. (1) [i.e., $\mathbf{N}(\mathbf{u}) = \mathbf{0}$] admits the following Kelvin-mode solution [44–46],

$$\mathbf{u} = \hat{\mathbf{u}}(t)e^{i\mathbf{k}\cdot\mathbf{x}}, \tag{2a}$$

where $\mathbf{x} = (x, y, z)$ and $\mathbf{k} = (\kappa_1, \kappa_2, \kappa_3)$ is the wave vector with κ_1, κ_2, and κ_3 being the dimensionless streamwise, cross-stream, and spanwise wave numbers, respectively. Here, κ_1 and κ_3 are constants to be prescribed, whereas $\kappa_2(t) = \kappa_{2,0} - \kappa_1 t$ is a linear function in time where $\kappa_{2,0}$ is a constant to be given. We note that Eq. (2) can be rearranged as

$$\mathbf{u} = \hat{\mathbf{u}}(t)e^{i[\kappa_1(x-Ut)+\kappa_{2,0}y+\kappa_3 z]}, \tag{2b}$$

with U ($=y$) being the streamwise base-flow velocity. This form of the solution suggests that $\hat{\mathbf{u}}(t)$ is merely a Fourier mode of $\mathbf{u}$ in the comoving frame with the local base flow, and the linear time dependence in $\kappa_2(t)$ originates from the downstream advection of the perturbation velocity due to the base flow with shear.

The length and velocity scales of the flow can now be defined such that $\mathcal{L} = 1/\kappa^*_{2,0}$ and $\mathcal{U} = S^*/\kappa^*_{2,0}$, where $\kappa^*_{2,0}$ (>0) is the dimensional form of $\kappa_{2,0}$ and S^* is the shear rate of the base flow. This yields $\kappa_2(t) = 1 - \kappa_1 t$ and $\mathrm{Re} = S^*/[\nu(\kappa^*_{2,0})^2]$. Also, $\hat{\mathbf{u}}(t)$ in Eq. (2) is obtained as [47]

$$\hat{u}(t) = \hat{u}_0 e^{\phi(t)} - \hat{v}_0\kappa_1\left(\frac{\kappa_0^2\kappa_2(t)}{\kappa_h^2\kappa^2(t)}\right)e^{\phi(t)} - \hat{v}_0\left(\frac{\kappa_0^2\kappa_3^2[\theta(t)-\theta(0)]}{\kappa_1\kappa_h^3}\right)e^{\phi(t)}, \tag{3a}$$

$$\hat{v}(t) = \frac{\hat{v}_0\kappa_0^2}{\kappa^2(t)}e^{\phi(t)}, \tag{3b}$$

$$\hat{w}(t) = \hat{w}_0 e^{\phi(t)} - \hat{v}_0\kappa_3\left(\frac{\kappa_0^2\kappa_2(t)}{\kappa_h^2\kappa^2(t)}\right)e^{\phi(t)} + \hat{v}_0\left(\frac{\kappa_0^2\kappa_3[\theta(t)-\theta(0)]}{\kappa_h^3}\right)e^{\phi(t)}, \tag{3c}$$

where $\hat{\mathbf{u}}_0 = (\hat{u}_0, \hat{v}_0, \hat{w}_0)$ is the initial condition, $\kappa(t) = [\kappa_1^2 + \kappa_2^2(t) + \kappa_3^2]^{1/2}$, $\kappa_0 = \kappa(0)$, and $\kappa_h = (\kappa_1^2 + \kappa_3^2)^{1/2}$. Also,

$$\theta(t) = \arctan\left(\frac{\kappa_h}{\kappa_2(t)}\right), \quad \phi(t) = -\frac{1}{\mathrm{Re}}\int_0^t \kappa^2(\tau)d\tau, \tag{3d}$$

where $\theta(t) \in [0, \pi)$ is the angle between the horizontal (κ_h) and vertical (κ_2) wave-vector components, equivalent to the clockwise inclination angle of the wave from the horizontal plane, and $\phi(t)$ incorporates the effect of viscosity into the time evolution of the solution.

Now, we briefly summarize the physical implications of Eq. (3) (see also Ref. [47]). For simplicity, we shall also assume $\hat{u}_0 = 0$ and $\hat{w}_0 = 0$ because they do not contribute to any growth of the perturbation kinetic energy. Depending on κ_1 and κ_3, the dominant physical mechanisms at play can be classified into the following three categories:

(1) Lift-up effect ($\kappa_1 \to 0$). In the limit of $\kappa_1 \to 0$, the term which primarily contributes to the perturbation kinetic energy is the last term on the right-hand side of Eq. (3a). This term is also the particular solution of $\hat{u}$ to the Squire's equation obtained from the homogeneous solution to the Orr-Sommerfeld equation, describing the lift-up effect of streamwise velocity [47]. In the inviscid limit ($\mathrm{Re} \to \infty$), it also yields $\hat{u}(t) \sim t$ for $t \ll \mathrm{Re}$, retrieving the algebraic instability in Ref. [4].

(2) Orr mechannism ($\kappa_3 = 0$). In this case, Eq. (3) is simplified into

$$\hat{u}(t) = -\hat{v}_0 \kappa_0^2 \frac{\kappa_1 \kappa_2(t)}{\kappa_h^2 \kappa^2(t)} e^{\phi(t)}, \quad \hat{v}(t) = \frac{\hat{v}_0 \kappa_0^2}{\kappa^2(t)} e^{\phi(t)}, \tag{4}$$

which stems from the homogeneous solution to the Orr-Sommerfeld equation [47]. Since $\phi(t) < 0$ for $t > 0$, Eq. (4) implies that having a decreasing $\kappa^2(t)$ in time is an important way to achieve an energy growth, and, in particular, this is the only way for $\hat{v}(t)$ to do so. Given the form of $\kappa_2(t)(= 1 - \kappa_1 t)$, $\kappa^2(t)$ decreases for $t < 1/\kappa_1$ and reaches its minimum at $t = 1/\kappa_1$. $\kappa^2(t)$ then increases in time for $t > 1/\kappa_1$. We note that $\theta_0 < \theta(t) < \pi/2$ (upstream inclined wave) for $t < 1/\kappa_1$, whereas $\pi/2 < \theta(t) < \pi$ (downstream inclined wave) for $t > 1/\kappa_1$. This implies that $\kappa^{-2}(t)$ in Eq. (4) describes the Orr mechanism, by which the maximum perturbation energy would be achieved around $t = 1/\kappa_1$. Finally, it is worth mentioning that the (linear) time dependence of $\kappa_2(t)$ originates from the presence of the shear in base flow, as is indicated by Eq. (2b). This confirms that the Orr mechanism is indeed a process driven by the shear in base flow.

(3) Lift-up effect induced by the Orr mechanism ($\kappa_1 \neq 0$ *and* $\kappa_3 \neq 0$). Given the discussion above for the two limiting cases (i.e., $\kappa_1 \to 0$ and $\kappa_3 = 0$), the lift-up effect is described by the last terms with $\theta(t)$ in Eqs. (3a) and (3c), while the Orr mechanism would be described by those with $\kappa^{-2}(t)$ in Eq. (3). For $\kappa_1 \neq 0$ and $\kappa_3 \neq 0$, the two mechanisms coexist, as none of the related terms vanish. Given the form of Eq. (3), the Orr mechanism would operate as described above, and it extends to $\hat{w}$ in the same manner. However, in this case, some care needs to be taken for the interpretation of the lift-up effect because the time dependence of $\theta(t)$ now contributes to the related terms. For $\kappa_1 \neq 0$, $[\theta(t) - \theta(0)]$ in Eq. (3) now increases monotonically from zero and approaches asymptotically its upper bound $[\pi - \theta(0)]$ as $t \to \infty$. The gradually increasing $\theta(t)$ activates the last terms in Eqs. (3a) and (3c), implying that the lift-up effect in this case is induced by the Orr mechanism—otherwise, those terms in Eqs. (3a) and (3c) would remain zero, since $\theta(t) = \theta(0)$ for all $t > 0$ in the absence of the Orr mechanism. It is also important to mention that this effect is particularly well described by $\hat{w}$, because, for a given κ_1 and κ_3, the energy growth in time by the lift-up term in Eq. (3c) is only affected by $\theta(t)$—in the case of $\hat{u}$, the aspect ratio of the perturbation (i.e., κ_3/κ_1) is another factor affecting the extent of amplification. This indicates that the spanwise velocity would be the best observable to measure this effect.

To more quantitatively capture the physical mechanisms discussed above, the linear optimal energy growth is formulated for given κ_1 and κ_3,

$$G(t; \kappa_1, \kappa_3) = \max_{\mathbf{u}_0 \neq 0} \frac{||\mathbf{u}(t)||^2}{||\mathbf{u}_0||^2}, \tag{5a}$$

where $||\mathbf{u}||^2 = (1/V_\Omega) \int_\Omega \mathbf{u}^H \mathbf{u} \, dV$ (the superscript H indicates complex conjugate transpose) with $\mathbf{u}_0 = \mathbf{u}(0)$, $\Omega = [0, 2\pi/\kappa_1) \times [0, 2\pi) \times [0, 2\pi/\kappa_3)$, and V_Ω being the volume of Ω. Given the discussion above, it would also be useful to introduce the following componentwise optimal transient growth, which shares a similar idea with Refs. [18,48] where the observable of interest is considered for the objective functional of the optimization, i.e.,

$$G_{u_i}(t; \kappa_1, \kappa_3) = \max_{\mathbf{u}_0 \neq 0} \frac{||u_i(t)||^2}{||\mathbf{u}_0||^2}, \tag{5b}$$

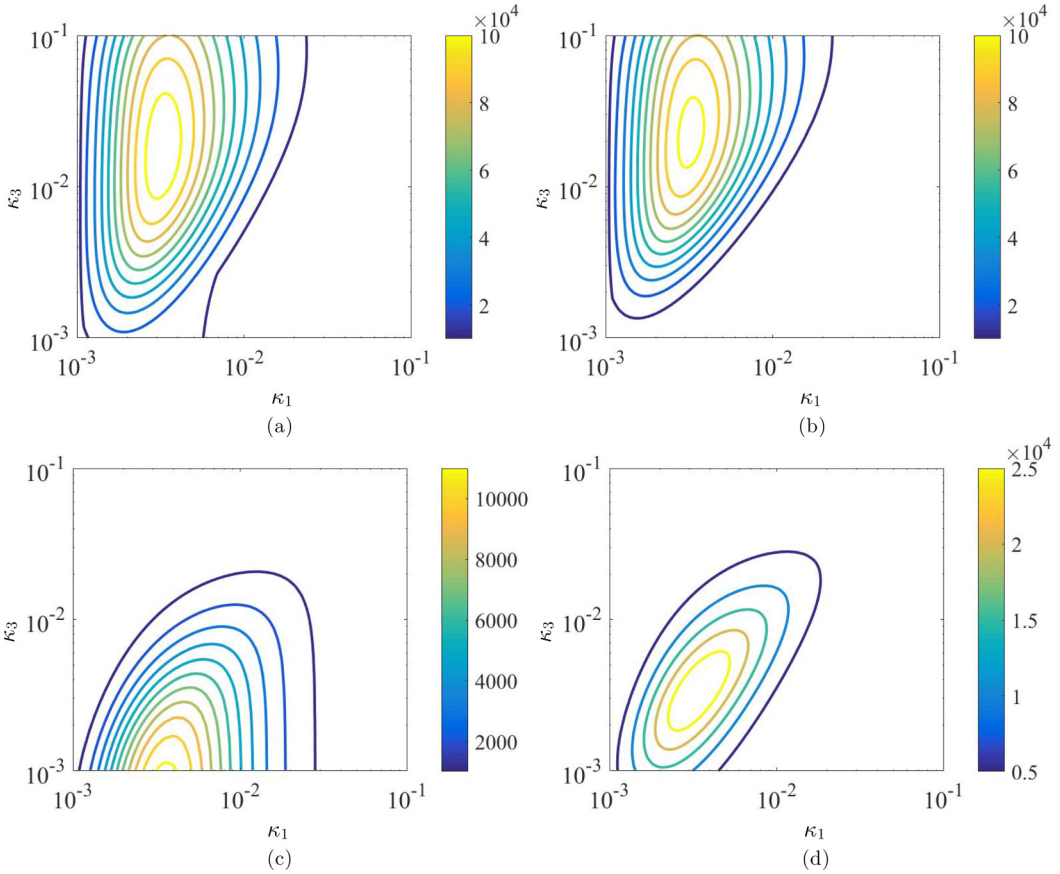

FIG. 1. Contours of (a) $G_{\max}$, (b) $G_{u,\max}$, (c) $G_{v,\max}$, and (d) $G_{w,\max}$ in the κ_1-κ_3 plane for Re $= 100$.

where $||u_i||^2 = (1/V_\Omega)\int_\Omega |u_i|^2 dV$. By doing so, G_{u_1} (or G_u) would well characterize the energy amplification mostly by the lift-up effect, especially for $\kappa_1 \to 0$. Similarly, G_{u_2} (or G_v) would do the same for the Orr mechanism predominant at $\kappa_3 = 0$. Finally, G_{u_3} (or G_w) would well identify the energy amplification via the lift-up effect induced by the Orr mechanism.

The optimization problem Eq. (5) is easily solved using the analytical solution Eq. (3). Once the solution to Eq. (5) is obtained, the maximum energy growth is further sought over the time, i.e., $G_{\max}(\kappa_1, \kappa_3) = \max_t G(t; \kappa_1, \kappa_3)$ and $G_{u_i,\max}(\kappa_1, \kappa_3) = \max_t G_{u_i}(t; \kappa_1, \kappa_3)$. Figure 1 shows the contours of $G_{\max}$ and $G_{u_i,\max}$ on the κ_1-κ_3 plane, where $G_{\max}$ and $G_{u,\max}$ are quite similar to each other. This suggests the importance of the lift-up effect in the amplification of the streamwise velocity. However, $G_{\max}$ and $G_{u,\max}$ do show some difference for some κ_1 and κ_3, and it is pronounced especially for small κ_3 (i.e., $\kappa_3 \simeq 10^{-3}$). In fact, $G_{v,\max}$ exhibits its peak at $\kappa_3 \simeq 10^{-3}$. This indicates that the difference is caused by the contribution of the Orr mechanism to $G_{u,\max}$ being smaller than the contribution to $G_{\max}$ for small κ_3. Finally, $G_{w,\max}$ shows its peak between the peak locations of $G_{u,\max}$ and $G_{v,\max}$, consistent with the expected nature of $G_{w,\max}$, which would well characterize the lift-up effect induced by the Orr mechanism.

The typical features of the optimal transient growth observed in wall-bounded shear flows [27,47] are also well observed, if a sufficiently large κ_3 is considered. Figure 2 shows the variations of $G_{\max}$ and $G_{u_i,\max}$ with κ_1 for a given $\kappa_3 = 10^{-2}$ at Re $= 100$. The results show that the behaviors of $G_{\max}$ and $G_{u,\max}$ with κ_1 are very similar. Furthermore, the peaks of $G_{\max}$ and $G_{u,\max}$ are obtained with κ_1 much smaller than those at which the peaks of $G_{v,\max}$ and $G_{w,\max}$ are achieved. This indicates that

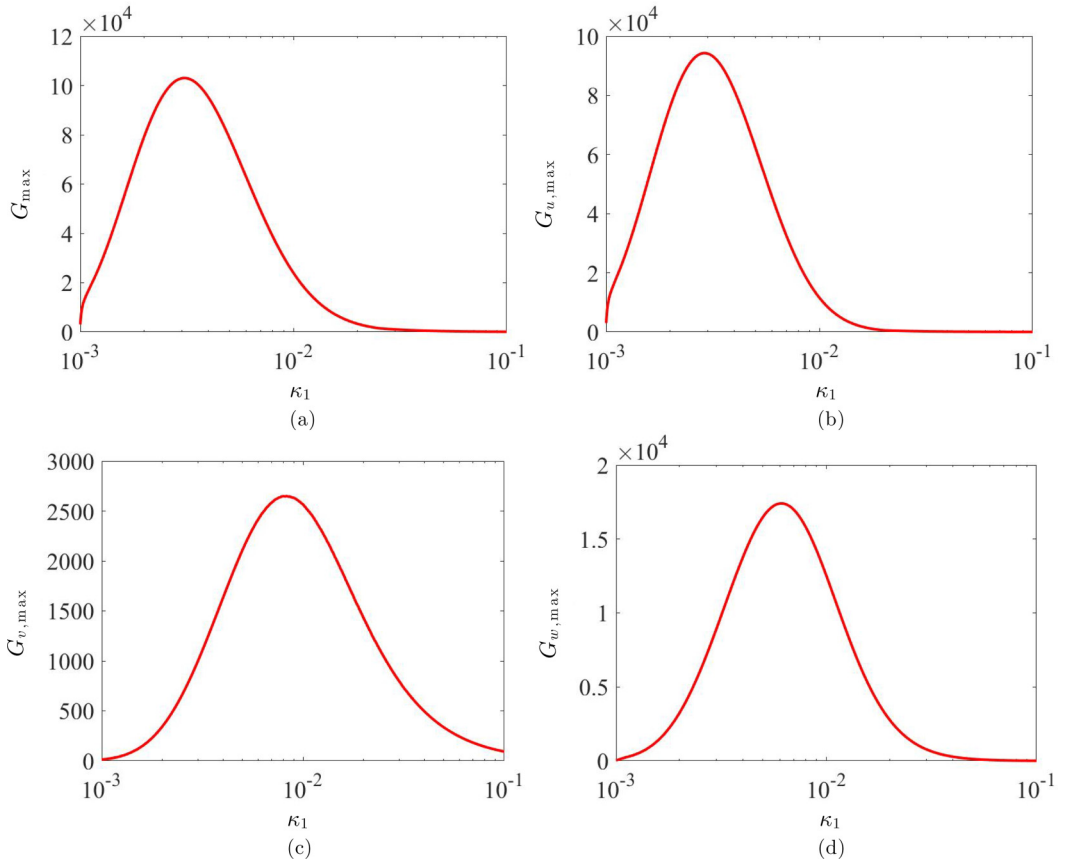

FIG. 2. Variation of (a) $G_{\max}$, (b) $G_{u,\max}$, (c) $G_{v,\max}$, and (d) $G_{w,\max}$ with κ_1 for $\kappa_3 = 10^{-2}$ and $\mathrm{Re} = 100$.

the lift-up effect for the streamwise velocity is predominant for streamwise elongated perturbations, consistent with many previous studies [2,3,7,8].

Finally, given the scope of the present study, the optimal initial condition maximizing the energy of spanwise velocity and the corresponding time traces of $||\mathbf{u}||^2$, $||u||^2$, $||v||^2$, and $||w||^2$ are visualized in Figs. 3 and 4. As expected, the optimal initial condition is tilted upstream and has a nonzero cross-stream velocity component forming rolls to trigger the lift-up effect (Fig. 3). The time evolution of $||\mathbf{u}||^2$, $||u||^2$, $||v||^2$, and $||w||^2$ shows that the growth of the total perturbation energy is dominated by the streamwise and spanwise components almost equally, i.e $||\mathbf{u}||^2 \simeq ||u||^2 + ||w||^2$ [Figs. 4(a), 4(c), and 4(d)]. However, it is the vertical component of the energy which achieves its maximum fastest [$t \simeq 300$ ($=1/\kappa_1$)], while the streamwise and spanwise ones reach their maximum later. We note that the short transient growth of $|v|^2$ should be the direct consequence of the Orr mechanism, because the form of $\hat{v}$ in Eq. (3b) admits only the Orr mechanism to play a role in the growth of $|v|^2$. Once the activation of the Orr mechanism is completed, the lift-up effect ensues with the nonzero cross-stream velocity component. Consequently, a significant transient energy growth of the streamwise and spanwise velocity perturbations arises for a long period, confirming the aforementioned discussion.

B. Plane Couette flow

Here, we briefly confirm the findings in Sec. II A in plane Couette flow. We note that the homogeneous shear flow and plane Couette flow share the same laminar base flow, which linearly

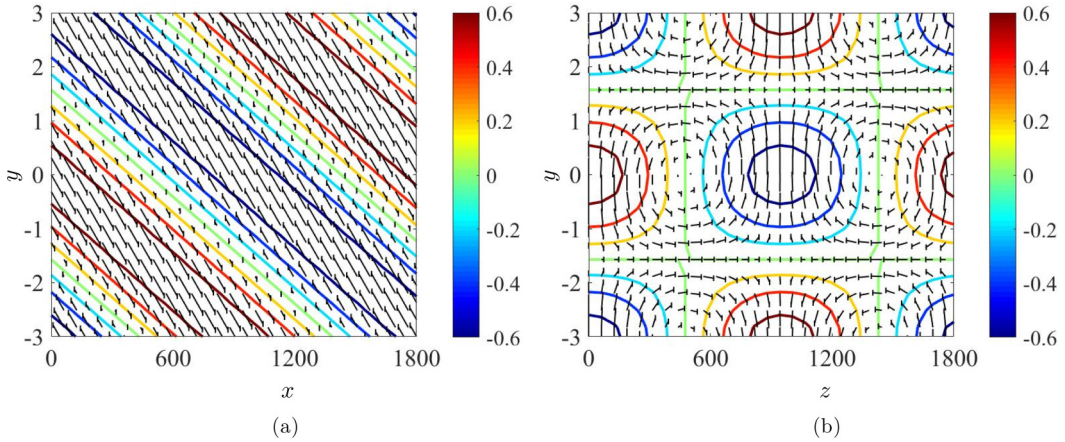

FIG. 3. The optimal initial condition maximizing the energy of spanwise velocity perturbation in the (a) x-y plane and (b) the y-z plane ($\kappa_1 = \kappa_3 = 0.0033$, $\mathrm{Re} = 100$). In (a), the contours denote w, and the vectors represent u and v. In (b), the contours denote u, and the vectors represent v and w. Here, the energy of the initial condition is normalized to unity.

depends on y. The only difference between the two is the boundary condition. Therefore, the two flows would share many similarities in the characteristics of their transient energy growth, as it essentially originates from the non-normality of the linearized Navier-Stokes equations. The dimensionless locations of two infinitely parallel plates are set to be at $y = \pm 1$, where y now becomes the wall-normal direction. The two walls move in opposite directions with the dimensionless velocity of $\mathbf{U} = (\pm 1, 0, 0)$. This implies that the flow variables are nondimensionalized by choosing the length scale $\mathcal{L}$ to be the half height of the channel and the velocity scale $\mathcal{U}$ to be the sliding speed of each plate. In the present study, $\mathrm{Re} = 400$ is considered.

A small-amplitude perturbation $\mathbf{u} = (u, v, w)$ is considered for the laminar Couette flow $\mathbf{U} = (y, 0, 0)$. Similarly to the uniform shear flow case, the Navier-Stokes equations linearized about $\mathbf{U} = (y, 0, 0)$ admit the plane Fourier-mode solution, $\mathbf{u} = \tilde{\mathbf{u}}(t, y)e^{i(\kappa_1 x + \kappa_3 z)}$, where $\tilde{\cdot}$ denotes the Fourier transform in the x and z directions. For each Fourier mode, the optimal perturbations for total energy and for each velocity component are computed by considering the optimization problems defined in Eqs. (5a) and (5b). The solutions to the optimization problems are obtained using the standard method [27]. The Orr-Sommerfeld and Squire system is discretized using a Chebyshev collocation method [49] with 120 collocation points in the wall-normal direction. The maximum energy growth and the corresponding optimal perturbation are computed by formulating a variational problem, the solution to which is obtained by singular value decomposition.

Given the expected similarity to the homogeneous shear flow discussed in Sec. II A, only $G_{u,\max}$ and $G_{w,\max}$ as a function of streamwise and spanwise wave numbers at $\mathrm{Re} = 400$ are shown in Fig. 5. We note that the optimal perturbations for $G_{u,\max}$ and $G_{w,\max}$ will be utilized in Sec. III to study the transition in plane Couette flow. As expected, the optimal perturbation for streamwise velocity is almost uniform in the streamwise direction [Fig. 5(a)]. On the contrary, the optimal perturbation for spanwise velocity appears as an oblique structure, the streamwise wave number of which is close to the spanwise one [Fig. 5(b)]. The time traces of $||u(t)||^2$ and $||w(t)||^2$, obtained from optimal perturbations for $G_{u,\max}$ and $G_{w,\max}$, are also shown in Fig. 6. Here, $\kappa_1 = 0$ and $\kappa_3 = 1.26$ are chosen for $G_{u,\max}$ and $\kappa_1 = 0.63$ and $\kappa_3 = 1.26$ are for $G_{w,\max}$. These wave-number pairs are not very far from those retaining the maxima of $G_{u,\max}$ and $G_{w,\max}$ in the κ_1-κ_3 plane (Fig. 5). In particular, $\kappa_1 = 0.63$ and $\kappa_3 = 1.26$ correspond to the fundamental wave numbers forming the spatial domain size of the direct numerical simulation (DNS) in Sec. III. For the optimal perturbation with $G_{u,\max}$ for $\kappa_1 = 0$ and $\kappa_3 = 1.26$, $||u(t)||^2$ shows a large amplification over a relatively long timescale

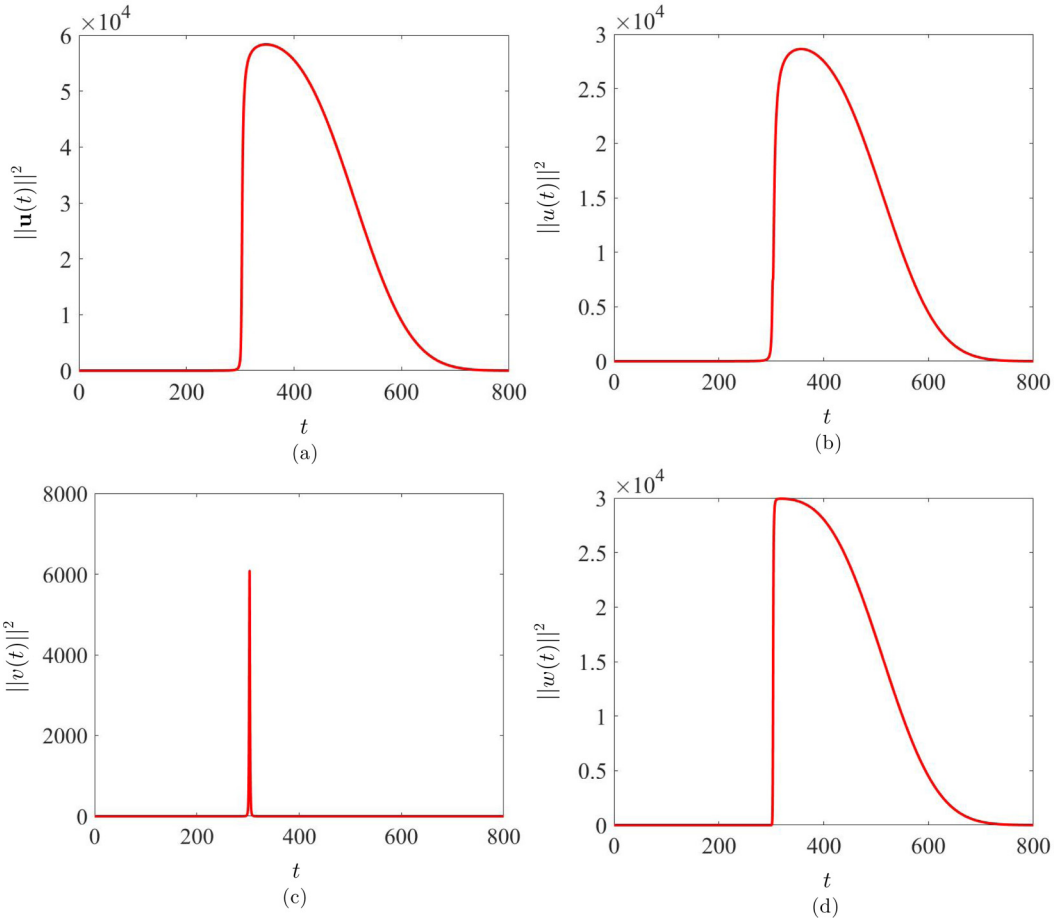

FIG. 4. The time dependence of (a) $||\mathbf{u}(t)||^2$, (b) $||u(t)||^2$, (c) $||v(t)||^2$, and (d) $||w(t)||^2$ for $\kappa_1 = \kappa_3 = 0.0033$ (Re $= 100$). Here, the initial condition is given by the optimal perturbation maximizing the energy of spanwise velocity.

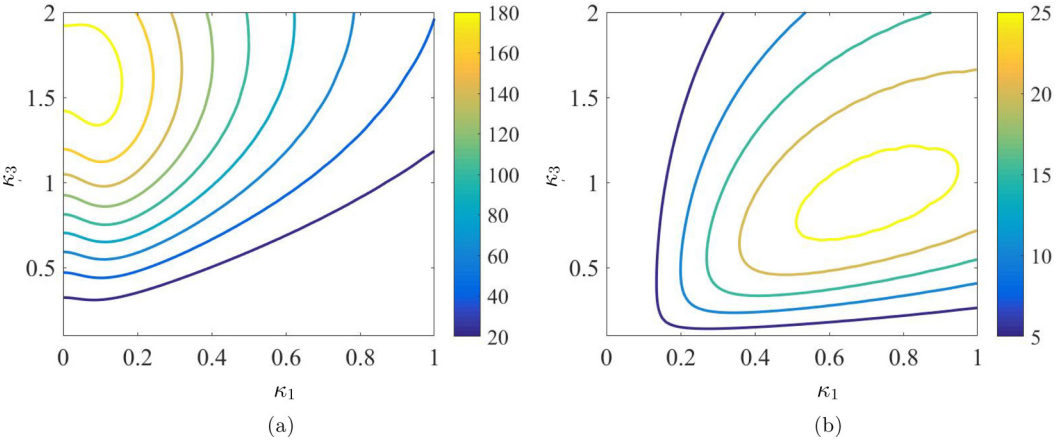

FIG. 5. The contours of (a) $G_{u,\max}$ and (b) $G_{w,\max}$ in terms of κ_1 and κ_3 at Re $= 400$.

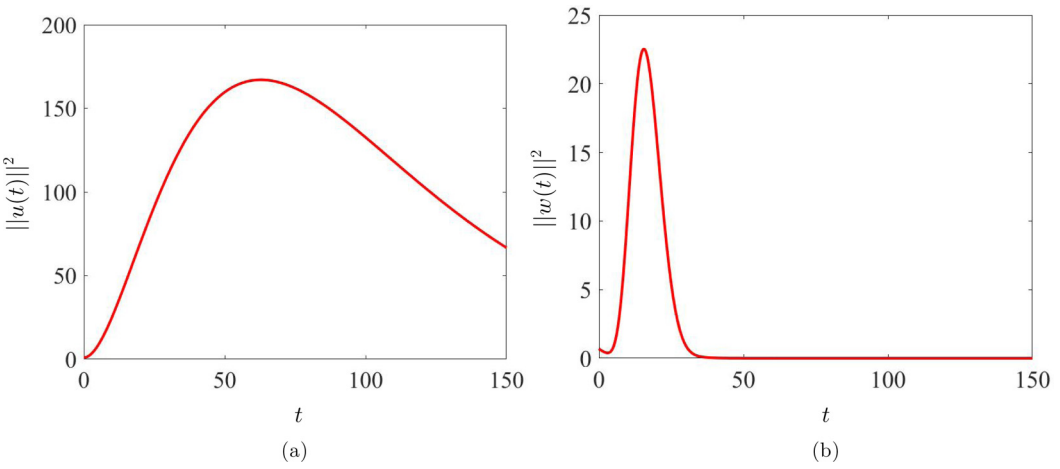

FIG. 6. Temporal evolution of (a) $||u(t)||^2$ from the optimal initial condition for $G_{u,\max}$ ($\kappa_1 = 0$, $\kappa_3 = 1.26$), and (b) $||w(t)||^2$ from the one for $G_{w,\max}$ ($\kappa_1 = 0.63$, $\kappa_3 = 1.26$) at Re $= 400$.

of the evolution [Fig. 6(a)]. The amplification is mediated by the lift-up effect and involves the generation of the streaks (not shown). For the optimal perturbation with $G_{w,\max}$ for $\kappa_1 = 0.63$ and $\kappa_3 = 1.26$, $||w(t)||^2$ also exhibits a similar transient amplification [Fig. 6(b)]. However, in this case, the related maximum amplification of $||w(t)||^2$ is much smaller than that of $||u(t)||^2$ for $G_{u,\max}$, and the related timescale of the evolution is much shorter than that of $||u(t)||^2$ from $G_{u,\max}$. The time evolution from this initial condition is visualized in Fig. 7. The initial condition is inclined upstream [Fig. 7(a)]. The spanwise velocity evolved from this initial condition is tilted in the direction of

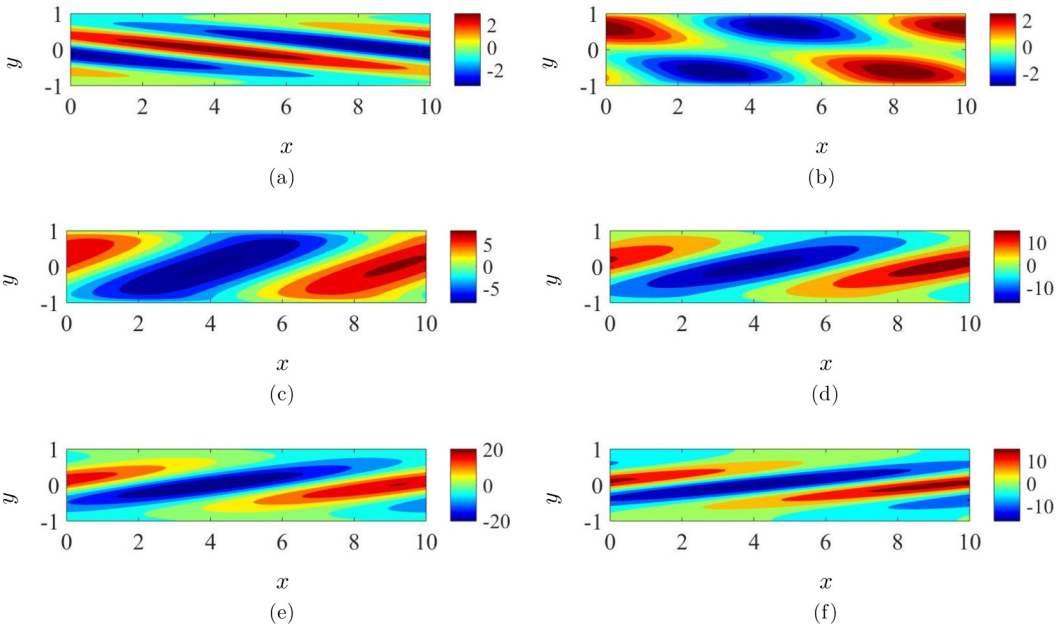

FIG. 7. Contours of spanwise velocity at (a) $t = 0$, (b) $t = 4$, (c) $t = 8$, (d) $t = 12$, (e) $t = 16$, (f) $t = 20$, and at $z = 0$ plane of the small-amplitude optimal spanwise velocity perturbation with $\kappa_1 = 0.63$, $\kappa_3 = 1.26$, Re $= 400$. Here, the energy of initial condition is normalized to unity.

the mean shear progressively, which gives an initial spurt to its transient amplification. The tilting angle becomes approximately orthogonal to the x axis around $t \simeq 6$ [Figs. 7(b) and 7(c)], at which the amplification solely by the Orr mechanism is expected to be most active from the homogeneous shear flow analysis [see Eq. (4)]. However, we note that $||w(t)||^2$ is still growing even at this instance and achieves it maximum around $t \simeq 20$ [Fig. 6(b)]. This is consistent with the behavior observed in the homogeneous shear flow (Fig. 4), indicating that the lift-up effect induced by the Orr mechanism is presumably responsible for the energy growth of the spanwise velocity for $t \gtrsim 6$.

III. THE ORR MECHANISM IN TRANSITION OF PLANE COUETTE FLOW

Now, the role of the Orr mechanism and the resulting lift-up effect in transition is studied in plane Couette flow with direct numerical simulation (DNS). In the present study, the DNS is performed using DIABLO [50], which has extensively been verified in previous studies [51]. In this numerical solver, the streamwise and spanwise directions are discretized by the Fourier-Galerkin method with the 2/3 rule for dealiasing, whereas the wall-normal direction is discretized by the second-order central finite-difference method. The fractional-step method is used for the time integration. More specifically, all the viscous terms are advanced in time with the Crank-Nicolson method, while the rest terms are integrated via a low-storage third-order Runge-Kutta method. The computational domain is chosen to be $L_x = 10$, $L_y = 2$, and $L_z = 5$ with the number of grid points $N_x = 32$, $N_y = 65$, and $N_z = 32$ in the streamwise, wall-normal, and spanwise directions, respectively. As a result, the fundamental wave numbers are given by $\kappa_{1,0} = 0.63$ and $\kappa_{3,0} = 1.26$, identical to those examined in Fig. 6(b). This then enables us to use the optimal perturbations given for G_u and G_w in Fig. 6 to build initial conditions for the DNS. As discussed in Sec. II A, the wave numbers for G_u and G_w in Fig. 6 are not very far from those resulting in the maxima of $G_{u,\max}$ and $G_{w,\max}$ in the κ_1-κ_3 plane. We note that the computational domain size is close to the one in which the Nagata's invariant solution emerges at the smallest Reynolds number ($\mathrm{Re}_c \simeq 127$) [52]. Also, in this domain, the developed turbulence typically exhibits a self-sustaining process involving a single low-speed (or high-speed) streak and the related quasistreamwise vortices [53], as the horizontal size of the domain in viscous inner units is not far from the minimal flow unit [54], i.e., $L_x^+ \simeq 360$ and $L_z^+ \simeq 180$, where the superscript $+$ indicates normalization by the viscous inner length scale. Lastly, it should be mentioned that the small computational domain is also deliberately considered to restrict us to study only the temporal evolution of the Orr-mechanism-induced transition dynamics. If a large computational domain was considered, transition experiences spatiotemporal complexities (e.g., the formation of turbulence spots and bands; see also the review by Ref. [55]) and this issue is beyond the scope of the present study.

A. Two transition scenarios with the Orr mechanism

In Sec. II, the optimal perturbation for spanwise velocity has been shown to exhibit a large amplification via the lift-up effect induced by the initial Orr mechanism. The large amplification of spanwise velocity implies that this type of initial condition may be utilized to efficiently trigger a secondary transient growth around the developed streaks [33], facilitating the streak transition scenario mentioned in Sec. I. However, it should also be pointed out that the optimal perturbation for the spanwise velocity exhibits a large amplification typically at the streamwise and spanwise wavelengths with $O(1)$ [Figs. 1(d) and 5(b)]. Therefore, the possibility of relating the oblique transition [42,43] to the Orr mechanism discussed above should also be considered. For this purpose, in the present study, we consider the following form of initial condition for the perturbation velocity,

$$\mathbf{u} = \lambda_1 \mathbf{u}_{\mathrm{opt}} + \lambda_2 \mathbf{u}_{\mathrm{opt},w}, \tag{6a}$$

where

$$\mathbf{u}_{\mathrm{opt}} = \mathrm{Re}[\tilde{\mathbf{u}}_{\mathrm{opt}}(y; 0, \kappa_{3,0}) e^{i\kappa_{3,0} z}], \tag{6b}$$

$$\mathbf{u}_{\mathrm{opt},w} = \mathrm{Re}[\tilde{\mathbf{u}}_{\mathrm{opt},w}(y; \kappa_{1,0}, \kappa_{3,0}) e^{i(\kappa_{1,0}x + \kappa_{3,0}z)} + \tilde{\mathbf{u}}_{\mathrm{opt},w}(y; \kappa_{1,0}, -\kappa_{3,0}) e^{i(\kappa_{1,0}x - \kappa_{3,0}z)}]. \tag{6c}$$

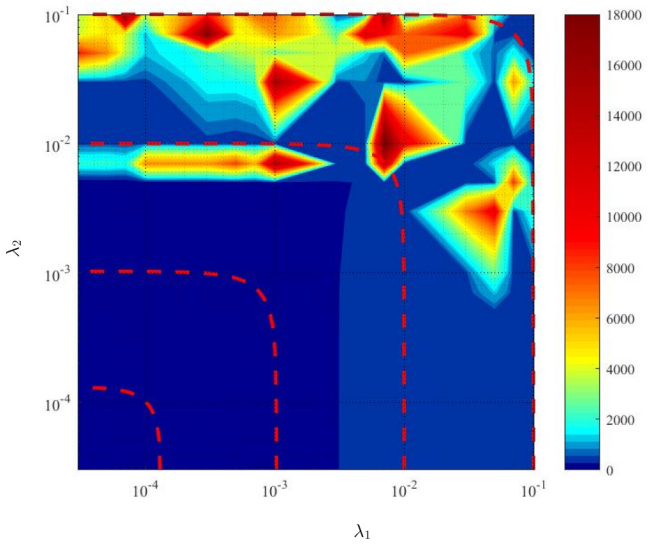

FIG. 8. Contours of lifetime T as a function of λ_1 and λ_2 at $\mathrm{Re} = 400$ in the log-log coordinates. Here, λ_1 and λ_2 are varied from 3×10^{-5} to 10^{-1}. The red dashed lines represent the initial disturbance energy, $E_0(=\lambda_1^2+\lambda_2^2) = 10^{-8}, 10^{-6}, 10^{-4}, 10^{-2}$.

Here, Re[·] denotes the real part, $\tilde{\mathbf{u}}_{\mathrm{opt}}$ and $\tilde{\mathbf{u}}_{\mathrm{opt},w}$ are the optimal perturbations for $G_{\max}$ and G_w, respectively, and they are obtained with $\kappa_{1,0} = 0.63$ and $\kappa_{3,0} = 1.26$. Also, $||\mathbf{u}_{\mathrm{opt}}||^2 = ||\mathbf{u}_{\mathrm{opt},w}||^2 = 1$ is set, such that λ_1 and λ_2 indicate the energies of the two optimal perturbations. This also leads the energy of the initial condition Eq. (6a) to be $E_0[\equiv ||\mathbf{u}(t=0)||^2] = \lambda_1^2+\lambda_2^2$. In the present study, λ_1 and λ_2 are varied from 3×10^{-5} to 10^{-1} to study the transition from the initial condition given in Eq. (6). We note that turbulence (chaotic state) with a small computational domain in plane Couette flow at $\mathrm{Re} = 400$ has a "finite lifetime" [56–58], as it is known as a "chaotic saddle" with the fractal boundary in the state space (i.e., the edge of turbulence). Due to this nature, here we characterize whether the flow reaches turbulence by defining the lifetime of each simulation. In the present study, the lifetime T is defined to be the duration from $t = 0$ to $t = T$, at which the total perturbation energy $E(\equiv ||\mathbf{u}||^2)$ becomes less than 10^{-5} for the first time. With this definition, the lifetimes for various combinations of λ_1 and λ_2 are computed and the corresponding results with 256 test cases are reported in Fig. 8.

Figure 8 shows that the lifetime distribution in the λ_1-λ_2 plane is indeed very irregular. This is due to the fractal nature of the boundary between the laminar and turbulent states. However, in general, if λ_1 and λ_2 are sufficiently large (say, $\lambda_1 \gtrsim 10^{-2}$ and $\lambda_2 \gtrsim 10^{-2}$), the lifetime can significantly increase ($T > 1000$). Further to this, Fig. 8 suggests that there are two ways to increase the lifetime. First, the lifetime can be quickly increased only with a relatively large value of λ_2 ($\approx7\times10^{-3}$). For diminishing small values of λ_1 ($<1\times10^{-3}$), this would correspond to the oblique transition scenario, since the pair of optimal oblique waves is much stronger than the optimal streamwise vortices at the initial time instant. Second, a transition can be triggered with a large λ_1 ($\geqslant10^{-2}$) and a relatively smaller λ_2 ($\leqslant5\times10^{-3}$) as well. This would be the streak transition case. Here, we can conclude that the initial disturbance energy E_0 required for the oblique transition is less than that for the streak transition. This issue will be addressed in Sec. III D.

B. Energy transfer in transition dynamics

To understand the time evolution of the dynamics of the two transition scenarios, we first introduce the time-dependent streamwise, wall-normal, and spanwise kinetic energies integrated

over the entire computational domain Ω,

$$E_{u_i} = \frac{1}{2V_\Omega}\int_\Omega u_i^2\, dV. \tag{7}$$

The streamwise, wall-normal, and spanwise kinetic energies of each plane Fourier mode are also considered,

$$E_{u_i}^{(m,n)} = \frac{1}{2}\int_{\Omega_y} \left|\tilde{u}_i^{(m,n)}\right|^2 dy, \tag{8a}$$

where $\Omega_y \in [-1, 1]$ and

$$u_i = \sum_m \sum_n \tilde{u}_i^{(m,n)}(t, y) e^{i[m\kappa_{1,0}x + n\kappa_{3,0}z]}. \tag{8b}$$

Given the streamwise domain size in the present study, the streaks are expected to be elongated over the entire streamwise domain. Therefore, further to Eqs. (7) and (8), the early-stage evolution of the streaks from the initial condition Eq. (6) is studied by considering the following perturbation energy equations for the streamwise-averaged variables integrated over the cross-streamwise domain $\Omega_{y,z} = [-1, 1]\times[0, 2\pi/\kappa_{3,0})$,

$$\frac{d}{dt}\left(\int_{\Omega_{y,z}} \frac{\langle u\rangle_x^2}{2}\, dS\right) = L + D_u + N_{u,y} + N_{u,z}, \tag{9a}$$

$$\frac{d}{dt}\left(\int_{\Omega_{y,z}} \frac{\langle v\rangle_x^2}{2}\, dS\right) = P_v + D_v + N_{v,y} + N_{v,z}, \tag{9b}$$

$$\frac{d}{dt}\left(\int_{\Omega_{y,z}} \frac{\langle w\rangle_x^2}{2}\, dS\right) = P_w + D_w + N_{w,y} + N_{w,z}, \tag{9c}$$

where the lift-up (or production) term is

$$L = -\int_{\Omega_{y,z}} \langle u\rangle_x \langle v\rangle_x \frac{dU}{dy} dS, \tag{9d}$$

the pressure transport/strain terms are

$$P_v = -\int_{\Omega_{y,z}} \langle v\rangle_x \frac{\partial\langle p\rangle_x}{\partial y}\, dS, \quad P_w = -\int_{\Omega_{y,z}} \langle w\rangle_x \frac{\partial\langle p\rangle_x}{\partial z}\, dS, \tag{9e}$$

the nonlinear transport terms for the streamwise component

$$N_{u,y} = -\int_{\Omega_{y,z}} \langle u\rangle_x \frac{\partial\langle uv\rangle_x}{\partial y} dS, \quad N_{u,z} = -\int_{\Omega_{y,z}} \langle u\rangle_x \frac{\partial\langle uw\rangle_x}{\partial z} dS, \tag{9f}$$

for the wall-normal component

$$N_{v,y} = -\int_{\Omega_{y,z}} \langle v\rangle_x \frac{\partial\langle vv\rangle_x}{\partial y}\, dS, \quad N_{v,z} = -\int_{\Omega_{y,z}} \langle v\rangle_x \frac{\partial\langle vw\rangle_x}{\partial z}\, dS, \tag{9g}$$

for the spanwise component

$$N_{w,y} = -\int_{\Omega_{y,z}} \langle w\rangle_x \frac{\partial\langle vw\rangle_x}{\partial y} dS, \quad N_{w,z} = -\int_{\Omega_{y,z}} \langle w\rangle_x \frac{\partial\langle ww\rangle_x}{\partial z} dS, \tag{9h}$$

and the viscous dissipation/transport terms are given by

$$D_u = \frac{1}{\mathrm{Re}}\int_{\Omega_{y,z}} \langle u\rangle_x \nabla^2_{y,z}\langle u\rangle_x \, dS, \quad D_v = \frac{1}{\mathrm{Re}}\int_{\Omega_{y,z}} \langle v\rangle_x \nabla^2_{y,z}\langle v\rangle_x \, dS,$$
$$D_w = \frac{1}{\mathrm{Re}}\int_{\Omega_{y,z}} \langle w\rangle_x \nabla^2_{y,z}\langle w\rangle_x \, dS. \tag{9i}$$

Here, $\langle\cdot\rangle_x$ indicates an average in the streamwise direction and $\nabla^2_{y,z} = \partial^2/\partial y^2 + \partial^2/\partial z^2$.

Once the streaks are sufficiently amplified, they break down through a streak instability and/or the related transient growth [28–31]. We note that the physical forms of the streak instability and the transient growth are very similar, since the transient growth is a consequence of the interaction with the least stable streak instability mode. In practice, their precise classification in a direct numerical simulation has been found to be very difficult [30]. As such, in the present study, the emergence of the streak instability and/or the transient growth is studied by computing the productions from the streaky flow [59],

$$T_y = -\int_\Omega \check{u}\check{v}\frac{\partial U_s}{\partial y} dV, \quad T_z = -\int_\Omega \check{u}\check{w}\frac{\partial U_s}{\partial z} dV, \tag{10}$$

where $\check{\mathbf{u}}[= (\check{u}, \check{v}, \check{w})] = \mathbf{u} - \langle\mathbf{u}\rangle_x$ and $U_s(y, z) = U(y) + \langle u\rangle_x$. Here, T_y is the production by wall-normal mean shear representing the activation of the varicose mode of the streak instability and/or transient growth, and T_z is the production by spanwise mean shear, indicating the sinuous mode [59].

C. Oblique transition

We first explore the roles of the Orr mechanism in the oblique transition by considering $\lambda_1 = 0.001$ and $\lambda_2 = 0.007$. The evolution of E_{u_i} and $E^{(m,n)}_{u_i}$, the instantaneous fields of streamwise velocity fluctuation for $t \in [0, 100]$, and the related energy transfer terms given in Eq. (9) are shown in Figs. 9–11, respectively. Given the form of the initial condition with $\lambda_2 > \lambda_1$, the (1,1) plane Fourier mode, which corresponds to $\mathbf{u}_{\mathrm{opt},w}$, first exhibits a notable energy growth for $t \in [0, 20]$ [blue dashed lines in Figs. 8(b)–8(d)]. In particular, $E^{(1,1)}_{u_2}$ grows for $t < 10$, and the growth of $E^{(1,1)}_{u_1}$ and $E^{(1,1)}_{u_3}$ subsequently appears for $10 < t < 20$ (see also Ref. [60]). The timescales here compare well with those in Fig. 6(b), indicating that the energy growth of the (1,1) mode is due to the Orr mechanism and the subsequent lift-up effect.

After the initial transient energy growth of the (1,1) mode, a large energy amplification of the (0,2) mode ensues through its streamwise component for $t \in [20, 30]$ [$E^{(0,2)}_{u_1}$; red dashed line in Fig. 9(b)]. This leads to the development of streamwise elongated streaks from the oblique-mode initial condition, as shown in Figs. 10(a)–10(c). We note that the large amplification of $E^{(0,2)}_{u_1}$ is primarily due to the linear amplification [L in Eq. (9d); black line in Fig. 11(a)], which can only be activated by the presence of nonzero $\tilde{u}^{(0,2)}_2$. Given the oblique-mode dominant nature of the initial condition, this implies that there must be a nonlinear mechanism for the generation of the (0,2) mode. Indeed, $E^{(0,2)}_{u_3}$ [red dashed line in Fig. 9(d)] is found to grow for $t \gtrsim 10$ due to the nonlinear transport $N_{w,z}$ [blue line in Fig. 11(c)] in this time interval [see also Eq. (9h)]. The amplification of the streamwise uniform spanwise velocity perturbation simultaneously activates the related pressure to enforce the continuity through the following Poisson equation:

$$\nabla^2_{y,z}\langle p\rangle_x = -\left[\frac{\partial^2\langle vv\rangle_x}{\partial y^2} + \frac{\partial^2\langle ww\rangle_x}{\partial z^2} + 2\frac{\partial^2\langle vw\rangle_x}{\partial y\partial z}\right]. \tag{11}$$

The pressure elevates the wall-normal pressure transport P_v [black line in Fig. 11(b) at $t \simeq 20$], which subsequently gives rise to the streamwise uniform wall-normal velocity fluctuation represented by $E^{(0,2)}_{u_2}$ [red dashed line in Fig. 9(c) at $t \simeq 20$ in relation to Eq. (9g)]. This ultimately leads to the emergence of streaks, and this process starting from the oblique-mode initial condition

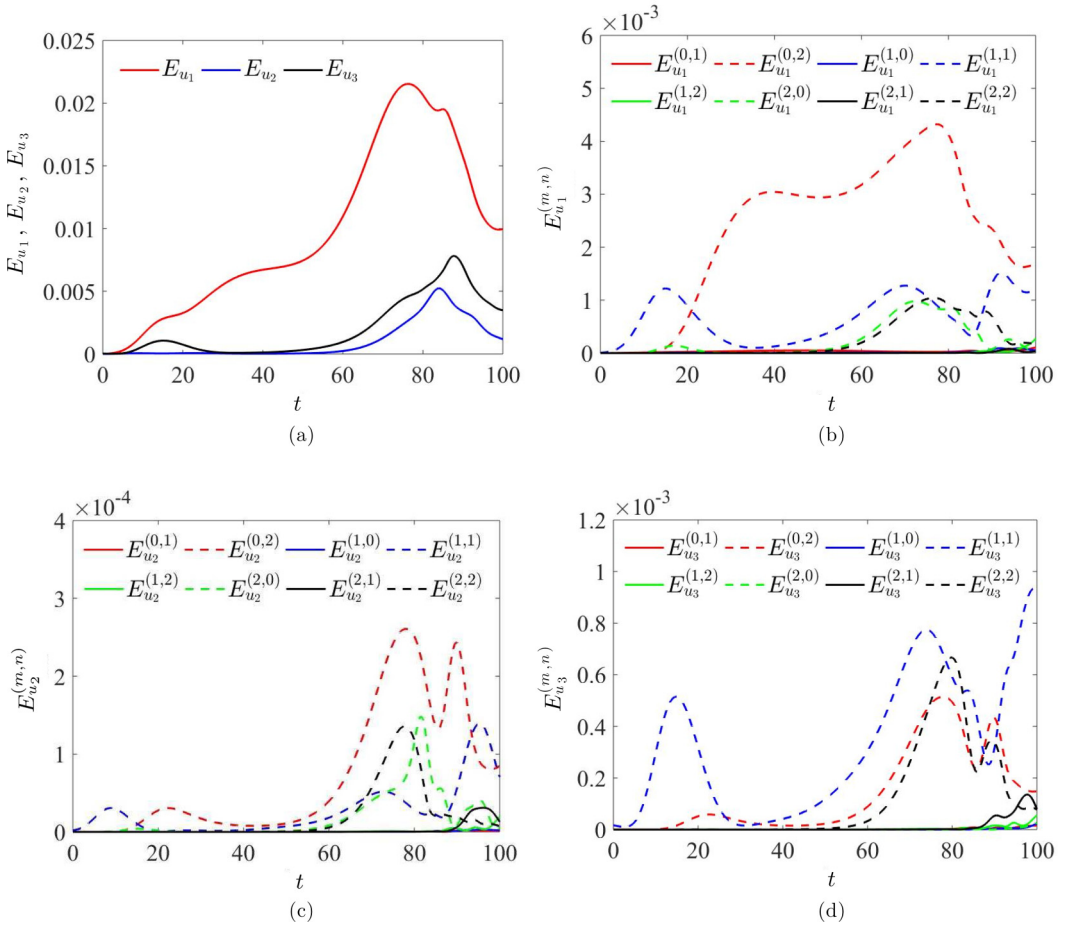

FIG. 9. The time evolution of (a) E_{u_1} (red), E_{u_2} (blue), E_{u_3} (black), (b) $E_{u_1}^{(m,n)}$, (c) $E_{u_2}^{(m,n)}$, and (d) $E_{u_3}^{(m,n)}$ for the initial condition given by Eq. (6) for $\lambda_1 = 0.001$ and $\lambda_2 = 0.007$ (Re = 400). In (b)–(d), red solid, $(m, n) = (0, 1)$; red dashed, (0,2); blue solid, (1,0); blue dashed, (1,1); green solid, (1,2); green dashed, (2,0); black solid, (2,1); black dashed, (2,2).

is a combined consequence of two linear mechanisms (i.e., Orr mechanism and lift-up effect), a nonlinear interaction of the spanwise velocity perturbation, and the continuity.

In the oblique transition, the influence of the Orr mechanism and the resulting lift-up effect is found not to be limited only at the early-stage transition (say, $t \lesssim 20$). At the late stage ($t \gtrsim 30$), the production terms T_y and T_z by the streaky flow in Eq. (10) gradually increase [Fig. 11(d)], resulting in the breakdown of the amplified streaks (see also Fig. 10). In particular, here, T_z is found to be greater than T_y, implying that the streak breakdown takes place through a sinuous mode. This is also seen very well in Figs. 10(c) and 10(d), where the emergence of a subharmonic sinuous-mode instability (or transient growth) is evident [29,31]. We note that the sinuous-mode breakdown of streaks has been understood to be highly receptive to the presence of the spanwise velocity perturbation [31,33], consistent with the form of T_z in Eq. (10). Indeed, a substantial amount of the energy of spanwise velocity perturbation is present even at $t \simeq 30$ [$E_{u_3}^{(1,1)}$; blue dashed line in Fig. 9(d)], although it has decayed due to the almost completed Orr mechanism for $20 \lesssim t \lesssim 30$. Once the streak instability (or transient growth) starts to develop, the spanwise velocity perturbation grows again, consistent

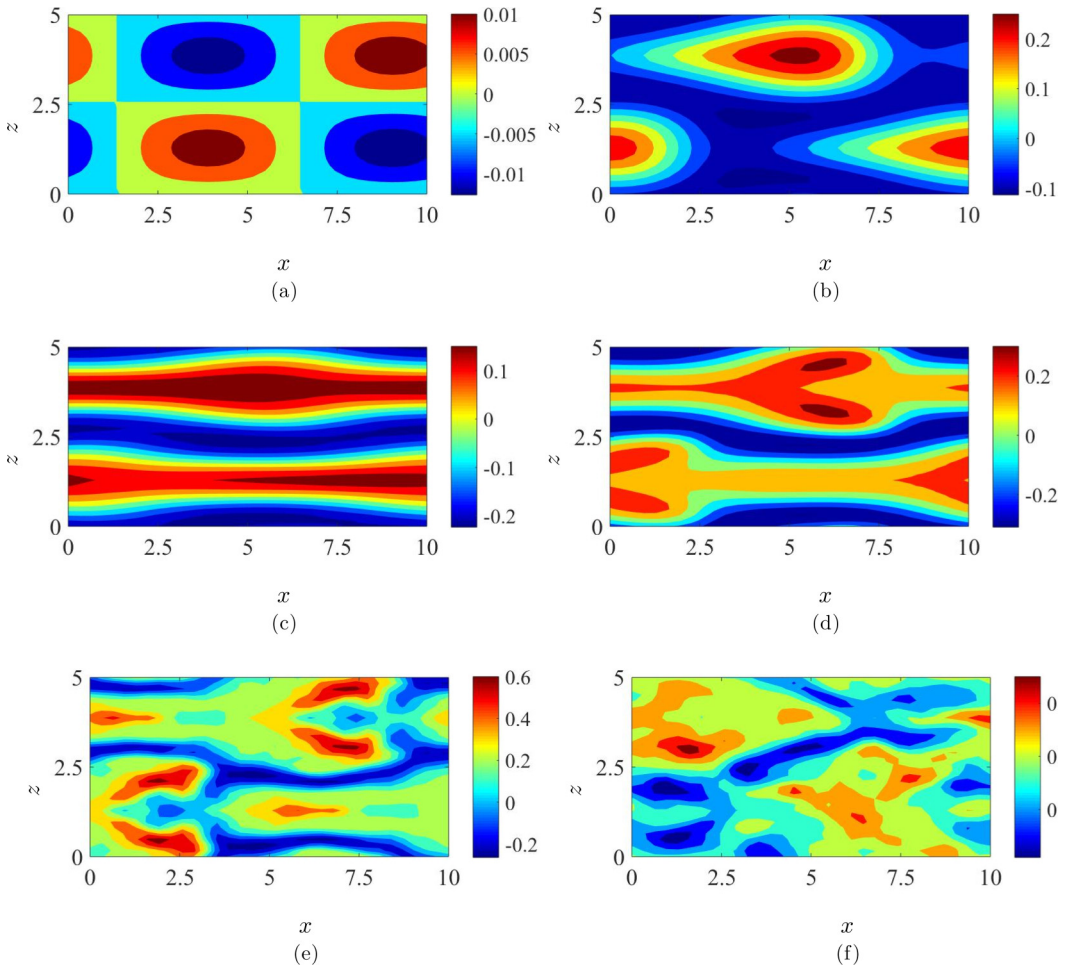

FIG. 10. Contours of streamwise velocity fluctuation on the plane of $y \approx 0.3$ at (a) $t = 0$, (b) $t = 20$, (c) $t = 40$, (d) $t = 60$, (e) $t = 80$, and (f) $t = 100$. Here, $\lambda_1 = 0.001$, $\lambda_2 = 0.007$, and $\mathrm{Re} = 400$.

with the growth of T_z in Eq. (10) [$E_{u_3}^{(1,1)}$; blue dashed line for $t \gtrsim 30$ in Fig. 9(d)]. The observation here suggests that the spanwise velocity perturbation, generated by the Orr mechanism at the early stage, plays the role of triggering the streak breakdown at the late stage—otherwise, it would also be difficult to explain the breakdown of the streaks especially through a "sinuous" mode, which is typically triggered by a spanwise velocity perturbation.

The DNS result suggests that the route to turbulence in the oblique transition is summarized as follows: (1) The Orr mechanism gives an initial spurt for the amplification of spanwise velocity perturbation by inducing the lift-up effect; (2) the amplified oblique spanwise velocity perturbation nonlinearly generates an elongated streamwise vortical motion together with continuity; (3) the streamwise vortical motion leads to streamwise elongated streaks with another lift-up effect; (4) the amplified streaks interact with the oblique spanwise velocity perturbation generated with the initial Orr mechanism; and (5) the streaks subsequently break down into turbulence. From this, it is evident that the spanwise velocity perturbation, generated by the Orr mechanism and the following lift-up effect at the early stage of transition, plays the key roles in initiating both streak amplification and breakdown, the two key processes in transition to turbulence.

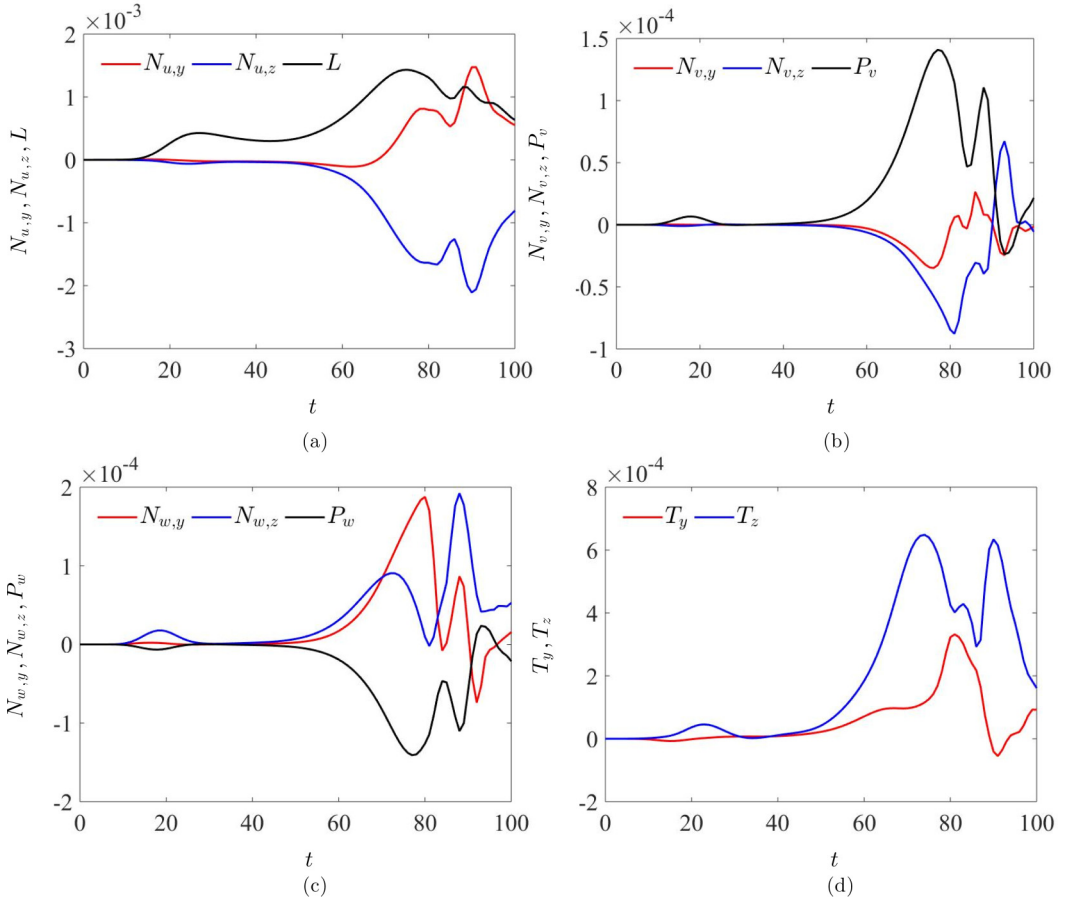

FIG. 11. Time traces of the energetics terms for the streak development and breakdown ($\lambda_1 = 0.001$ and $\lambda_2 = 0.007$): (a) $N_{u,y}$ (red), $N_{u,z}$ (blue), L (black); (b) $N_{v,y}$ (red), $N_{v,z}$ (blue), P_v (black); (c) $N_{w,y}$ (red), $N_{w,z}$ (blue), P_w (black); and (d) T_y (red), T_z (blue).

D. Streak transition

We now consider the other route of transition shown in Fig. 8 (i.e., streak transition for $\lambda_1 \gg \lambda_2$). The initial condition to be studied here is $\lambda_1 = 0.07$ and $\lambda_2 = 0.005$, implying that the initial condition is dominated by the optimal perturbation for the total velocity. The time traces of E_{u_i} and $E_{u_i}^{(m,n)}$, the instantaneous fields of streamwise velocity fluctuation for $t \in [0, 150]$, and the related energy transfer terms in Eq. (9) are presented in Figs. 12–14, respectively. As expected, there is a strong amplification of E_{u_1} and $E_{u_1}^{(0,1)}$ for $t \lesssim 20$ [red solid lines in Figs. 12(a) and 12(b)]. Indeed, the instantaneous flow fields show that streamwise-dependent structures at $t = 0$ due to small λ_2 are converted into the streamwise elongated streaks [Figs. 13(a) and 13(b)]. It is evident that the development of the streaks is due to the lift-up effect, as also confirmed by $L > 0$ during this time interval [black line in Fig. 14(a)]. When $t \simeq 20$, the stabilizing nonlinear terms $N_{u,y}$ and $N_{u,z}$ act strongly against the lift-up term L [Fig. 14(a)]. As a consequence, both E_{u_1} and $E_{u_1}^{(0,1)}$ begin to decay [red solid lines in Figs. 12(a) and 12(b)].

At the late stage ($t \gtrsim 30$), the wall-normal and spanwise velocity perturbations, which were decaying for $t \lesssim 30$, grow again [E_{u2} and E_{u3}; blue and black lines in Fig. 12(a)]. This is a consequence of the streak instability or transient growth. Indeed, as shown in Fig. 13(c), the

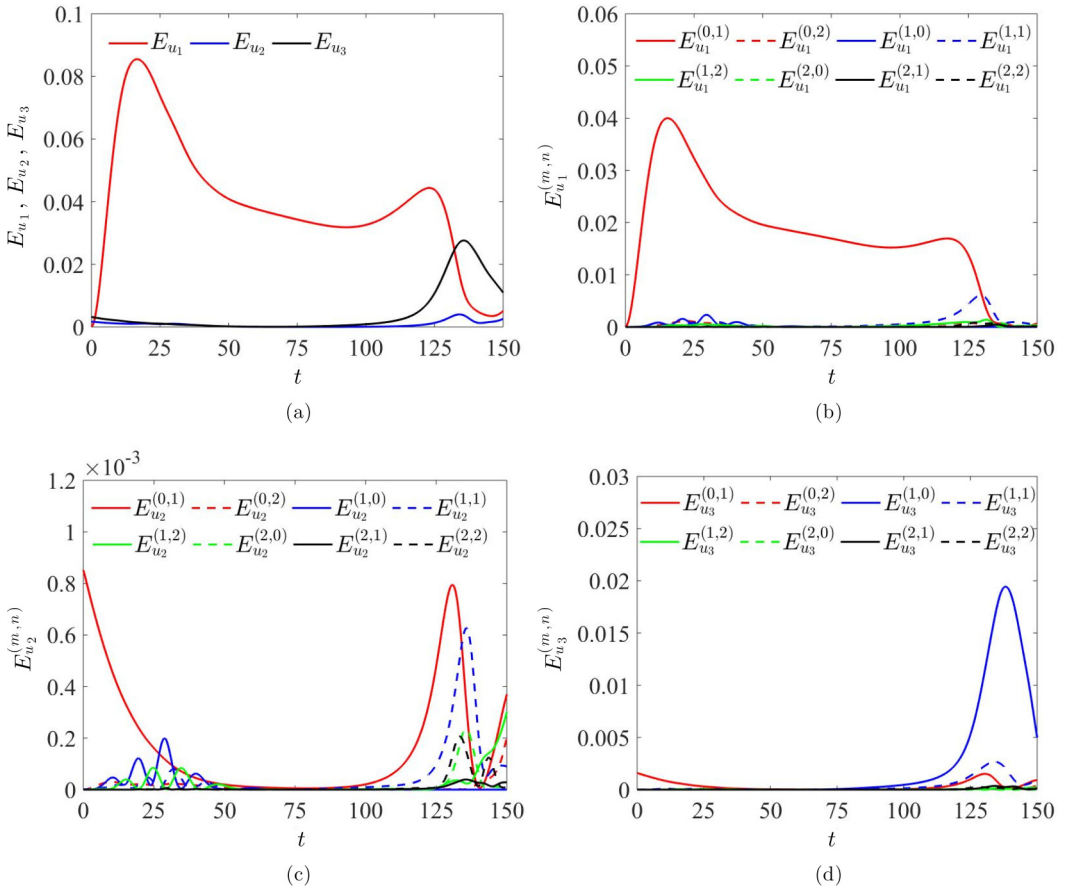

FIG. 12. Time traces of (a) E_{u_1} (red), E_{u_2} (blue), E_{u_3} (black), (b) $E_{u_1}^{(m,n)}$, (c) $E_{u_2}^{(m,n)}$, and (d) $E_{u_3}^{(m,n)}$ for the initial condition given by Eq. (6) for $\lambda_1 = 0.07$ and $\lambda_2 = 0.005$ (Re = 400). In (b)–(d): red solid, $(m, n) = (0, 1)$; red dashed, (0,2); blue solid, (1,0); blue dashed, (1,1); green solid, (1,2); green dashed, (2,0); black solid, (2,1); and black dashed, (2,2).

fundamental secondary instability starts to emerge with the streaks oscillating in a sinuous manner. The emergence of the fundamental sinuous mode is caused by the production by the spanwise shear of the streaky flow [59], and this is consistent with T_z being much greater than T_y [Fig. 14(b)]. Here, it is important to note that the fundamental sinuous mode responsible for the streak breakdown must be initiated by the spanwise velocity perturbation via the lift-up effect induced by the Orr mechanism at the early stage of transition: Indeed, the energy of spanwise velocity [E_{u3}; black line in Fig. 12(a)] and the related Fourier modes [Fig. 12(d)] are non-negligible at $t \simeq 30$, and, more importantly, a transition cannot take place if the amplitude of the oblique mode is too small (Fig. 8). The streaks eventually break down at $t \simeq 150$, and the flow subsequently becomes turbulent [Fig. 13(d)]. At this stage, the streamwise kinetic energy of the (0,1) mode reduces largely [red line in Fig. 12(b)], while the spanwise kinetic energy of the (1,0) mode is amplified significantly during the process [blue line in Fig. 12(d)].

The streak transition here is summarized to take the following route to turbulence: (1) The Orr mechanism initiates the growth of the spanwise velocity perturbation in the form of an oblique mode, but its effect is limited at the early stage; (2) instead, the optimal perturbation for all the velocity components, given in the form of elongated streamwise vortices, generates highly

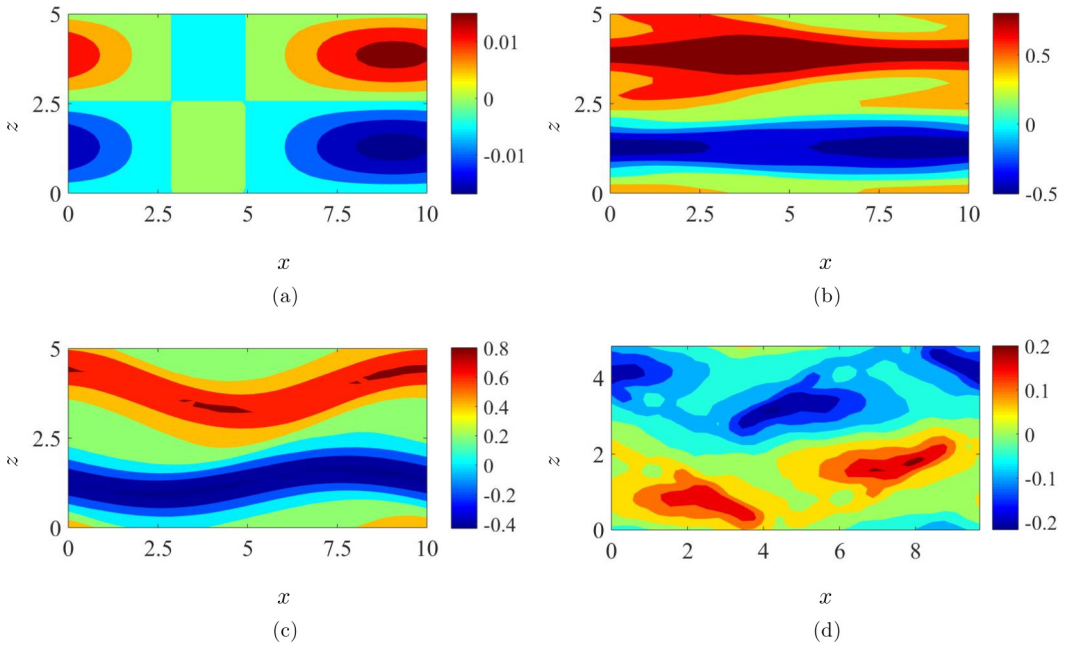

FIG. 13. Contours of streamwise velocity fluctuation on the plane of $y \approx 0.3$ at (a) $t = 0$, (b) $t = 20$, (c) $t = 120$, and (d) $t = 150$. Here, $\lambda_1 = 0.07$, $\lambda_2 = 0.005$, and $\mathrm{Re} = 400$.

amplified streamwise elongated streaks via the lift-up effect; (3) the streaks subsequently interact with the spanwise velocity structure given by the optimal perturbation for spanwise velocity; and (4) the streaks exhibit an instability and/or a transient growth and break down into turbulence. This transition scenario is almost identical to the one in Ref. [33]: The only difference is that the spanwise velocity perturbation in the present study is given by the oblique-mode optimal perturbation, whereas the one in Ref. [33] is driven externally by stochastic forcing.

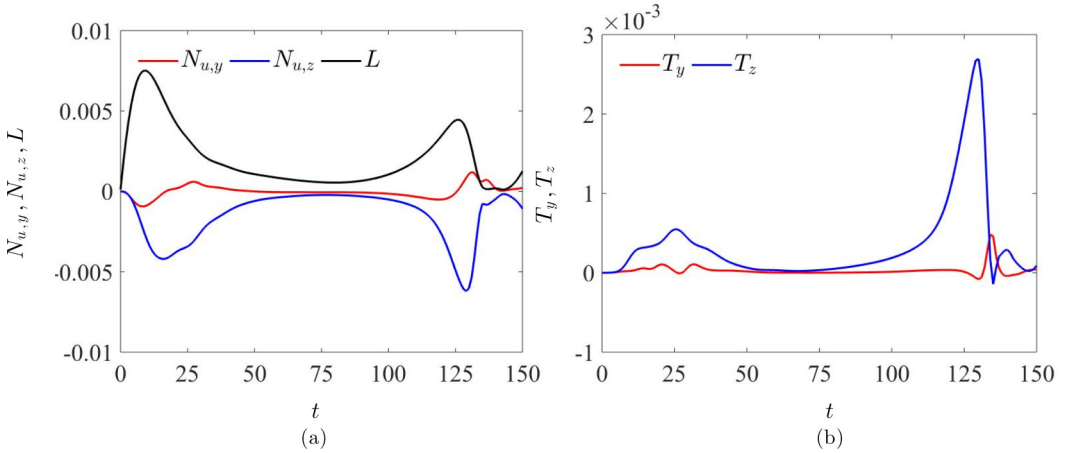

FIG. 14. Time traces of (a) $N_{u,y}$ (red), $N_{u,z}$ (blue), L (black), and (b) T_y (red line), T_z (blue) with $\lambda_1 = 0.07$, $\lambda_2 = 0.005$ at $\mathrm{Re} = 400$.

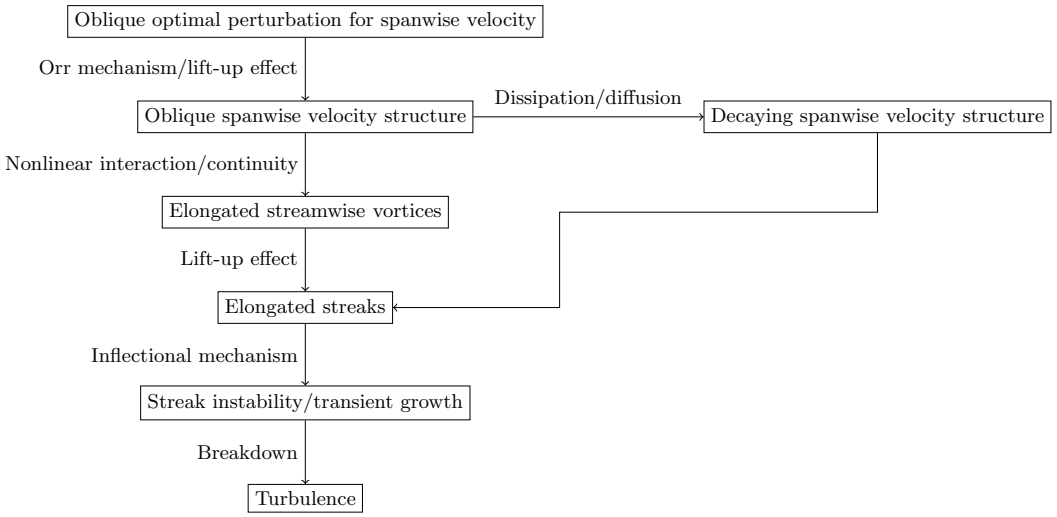

FIG. 15. A schematic diagram of how the Orr mechanism initiates the oblique transition.

Finally, the role of the Orr mechanism in the oblique transition (Sec. III C) is compared with the one in the streak transition here. In both transition scenarios, the most robust features are the emergence of streaks and their breakdown via a sinuous-mode instability (or transient growth). The subtle, but non-negligible, difference between the two transition scenarios essentially stems from the dynamics of the spanwise velocity perturbation. In the oblique transition, the spanwise velocity perturbation, generated by the Orr mechanism and the subsequent lift-up effect, not only nonlinearly interacts to generate streamwise vortical motions, but also initiates the breakdown of the amplified streaks into turbulence. However, in the streak transition, the role of the spanwise velocity perturbation is limited to the initiation of the streak breakdown. It is presumable that the multiple roles played by the spanwise velocity perturbation in both streak amplification and breakdown offer a more energetically efficient route to turbulence for the oblique transition at least for the initial conditions considered in the present study (see also Fig. 8). More importantly, the emergence of the Orr mechanism at the early stage and the following physical processes in the oblique transition are remarkably similar to those observed in the transition induced by the minimal seed [34–38]. In this respect, it should finally be mentioned that the nonlinear optimal perturbation calculated in the subspace spanned by the linear optimal perturbation modes has been shown to emerge in the form of an oblique mode [43], consistent with the findings in the present study.

IV. CONCLUDING REMARKS

In the present paper, the role of the Orr mechanism in the transition of plane Couette flow has been explored. We have first revisited the Orr mechanism in homogeneous shear flow and plane Couette flow and identified that the Orr mechanism induces a lift-up effect which significantly amplifies spanwise velocity. The optimal perturbation analysis for an individual velocity component reveals that the amplification of spanwise velocity is most active at the streamwise length comparable to the given spanwise length of the perturbation. The relevance of this mechanism to transition has subsequently been examined in plane Couette flow using DNS. In particular, we have considered a set of initial conditions by combining the optimal perturbation for spanwise velocity with the one for all the velocity components. The DNS results indicate that there are two representative transition scenarios: oblique and streak transitions. The schematic diagrams for the oblique and streak transitions are shown in Figs. 15 and 16. In the former, the spanwise velocity perturbation amplified by the Orr mechanism plays an initiating role in both streak amplification and breakdown,

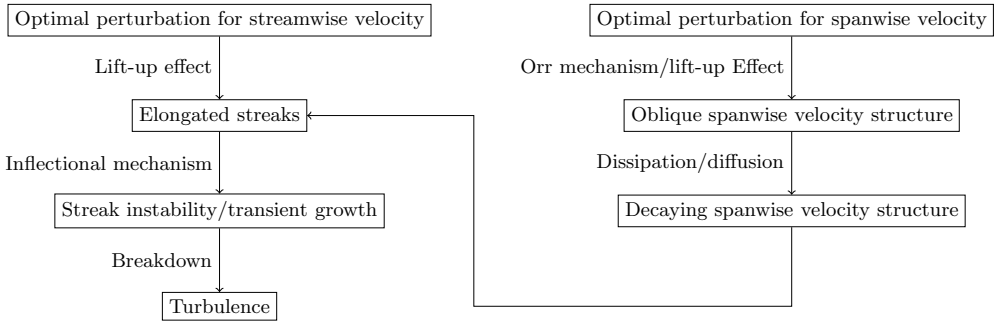

FIG. 16. A schematic diagram of how the Orr mechanism initiates the streak transition.

whereas in the latter, its role is limited only to the streak breakdown at the late stage of transition. As such, the oblique transition offers a route to turbulence energetically more efficient than the streak transition at least for the cases examined in the present study. Lastly, the oblique transition has been found to share many similarities to the one by the minimal seed [34–38].

The roles of the Orr mechanism identified in the present study are evidently for a highly idealized setting. However, these are also studied using optimal perturbations which lead to large transient energy growth. In this respect, it would be difficult to ignore their potential role even in realistic cases where initial condition may be given by a random noise. Indeed, our brief examination revealed that the role of the Orr mechanism is important in such cases (see Appendix A). Finally, the observations made for transition in the present study offer some important outlooks for the relevance of the Orr mechanism to fully developed turbulent flow. The existence of the Orr mechanism has repeatedly been reported by several previous studies [61–64]. These studies are primarily concerned with the generation of a wall-normal velocity structure via the Orr mechanism in relation to the self-sustaining process of the energy-containing eddies (or coherent structures) in wall-bounded turbulence [53,65–67]. However, the precise role and origin of the Orr mechanism in fully developed turbulence are still matters of debate: It was initially proposed that the Orr mechanism is a part of the self-sustaining process at a given length scale for the generation of the wall-normal velocity structure [61–63], but a recent study showed that the Orr mechanism can well be initiated by the wall-normal velocity structure originating from the energy cascade of "larger" energy-containing eddies [64]. In any case, it should be pointed out that all these investigations ignore the amplification

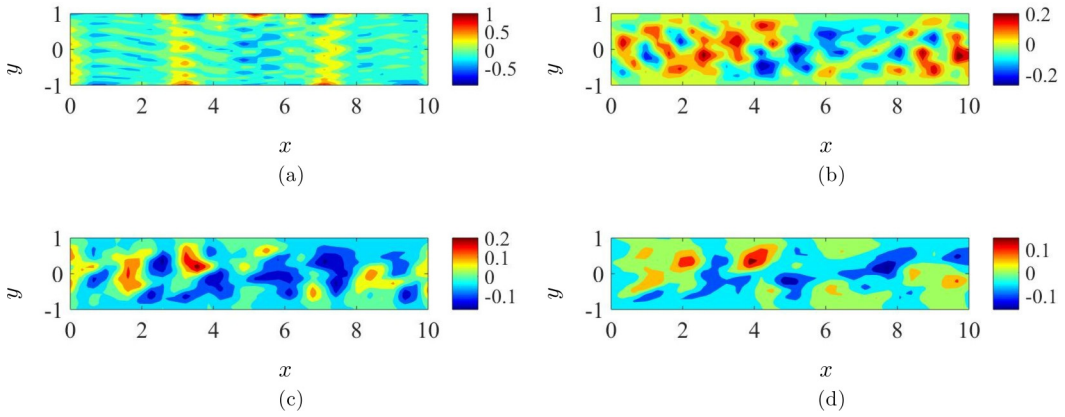

FIG. 17. Contours of the wall-normal velocity fluctuation at (a) $t = 0$, (b) $t = 2$, (c) $t = 4$, and (d) $t = 6$, and at the $z = 0$ plane of the small-amplitude random initial condition with $\mathrm{Re} = 400$.

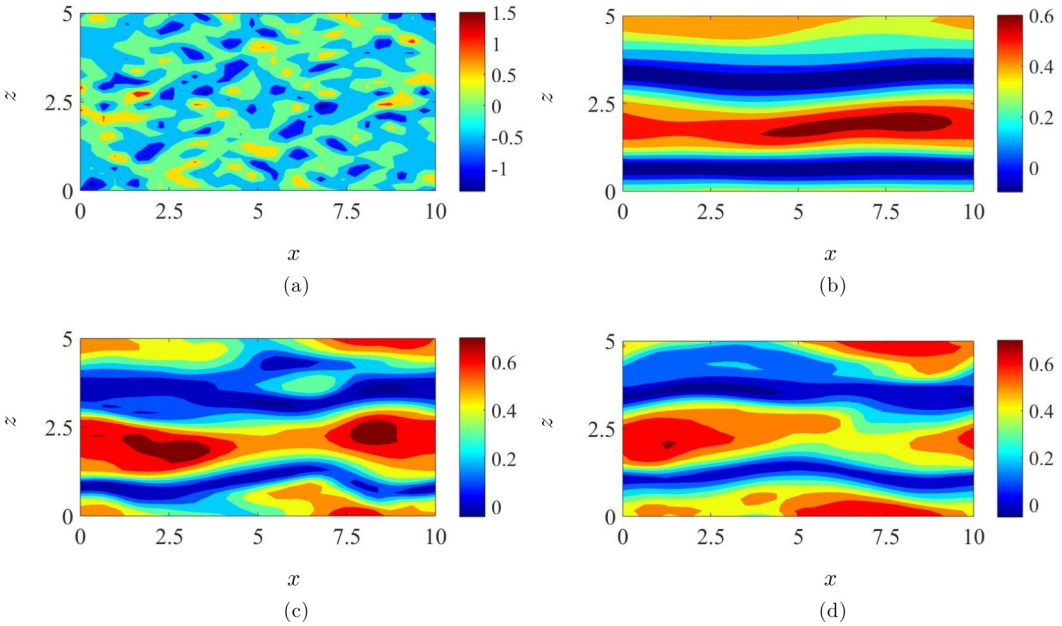

FIG. 18. Contours of the streamwise velocity fluctuation at (a) $t = 0$, (b) $t = 50$, (c) $t = 90$, and (d) $t = 100$, and at the $y \approx 0.3$ plane of the small-amplitude random initial condition with $\mathrm{Re} = 400$.

of the spanwise velocity structures caused by the lift-up effect following the Orr mechanism. Given the potential roles in the development and breakdown of streaks demonstrated for a transition in the present study, the significance of such spanwise velocity structures in fully developed turbulence should be investigated in the future.

APPENDIX A: TRANSITION FROM RANDOM INITIAL CONDITION

A DNS with a random initial condition is performed. The amplitude of the random initial condition is increased from a very small value to trigger a transition. The result indicates that the transition can be only induced with the initial condition energy $E_0 \approx 10^{-1}$. As expected, the initial

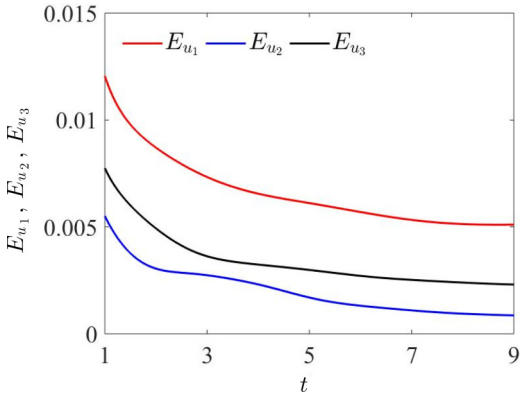

FIG. 19. The time evolution of E_{u_1} (red), E_{u_2} (blue), and E_{u_3} (black) with the random initial condition at $\mathrm{Re} = 400$.

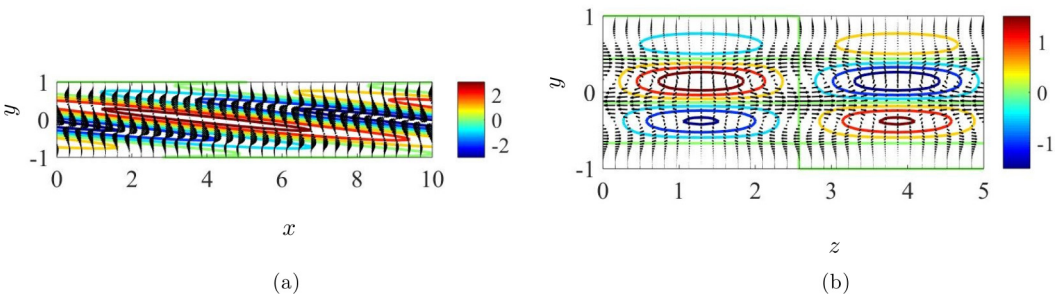

FIG. 20. The optimal initial condition maximizing the energy of spanwise velocity perturbation in the (a) x-y plane and (b) the y-z plane for plane Couette flow. ($\kappa_1 = 0.63, \kappa_3 = 1.25$, Re $= 400$). In (a), the contours denote w, and the vectors represent u and v. In (b), the contours denote u, and the vectors represent v and w. Here, the energy of the initial condition is normalized to unity.

condition energy required for a transition is much greater than that for the oblique transition as well as for the streak transition.

The time evolution from the random initial condition is visualized in Figs. 17 and 18. The random initial condition is isotropic at the initial time instant [Figs. 17(a) and 18(a)]. The wall-normal velocity evolved from this random initial condition is tilted in the mean-shear direction progressively, which indicates that the Orr mechanism does exist [Figs. 17(b)–17(d)]. This is also demonstrated by the time trace of the wall-normal kinetic energy in the early stage of the transition (blue line in Fig. 19). In particular, there is a slight growth for the wall-normal kinetic energy from $t \approx 2$. These imply that the Orr mechanism indeed gives an initial spurt to the transient amplification at the early stage of the transition with random initial condition.

The streaks are subsequently generated via the lift-up effect at later times [Figs. 18(b)–18(d)], and eventually break down in a sinuous manner to trigger a transition. However, given the meandering motion of the streaks in Fig. 18(c), it is difficult to determine whether the sinuous streak instability is fundamental or subharmonic. It appears that both exist in this case, indicating that both the spanwise noise in the initial condition and the Orr mechanism would play a role in the streak breakdown.

APPENDIX B: OPTIMAL PERTURBATION FOR SPANWISE VELOCITY IN COUETTE FLOW

The optimal initial condition maximizing the energy of spanwise velocity in plane Couette flow is shown in Fig. 20. The behavior is similar to that in the homogeneous shear flow, but with a little difference owing to the boundary condition (Fig. 3)—the optimal perturbation is tilted upstream, while containing the wall-normal velocity component which can induce the lift-up effect.

[1] L. H. Gustavsson, Energy growth of three-dimensional disturbances in plane Poiseuille flow, J. Fluid Mech. **224**, 241 (1991).

[2] K. M. Butler and B. F. Farrell, Three-dimensional optimal perturbations in viscous shear flow, Phys. Fluids A **4**, 1637 (1992).

[3] S. C. Reddy and D. S. Henningson, Energy growth in viscous channel flows, J. Fluid Mech. **252**, 209 (1993).

[4] T. Ellingsen and E. Palm, Stability of linear flow, Phys. Fluids **18**, 487 (1975).

[5] M. Landahl, A note on an algebraic instability of inviscid parallel shear flows, J. Fluid Mech. **98**, 243 (1980).

[6] M. Landahl, On sublayer streaks, J. Fluid Mech. **212**, 593 (1990).

[7] L. N. Trefethen, A. E. Trefethen, S. C. Reddy, and T. A. Driscoll, Hydrodynamic stability without eigenvalues, Science **261**, 578 (1993).
[8] P. J. Schmid and D. S. Henningson, Optimal energy density growth in Hagen–Poiseuille flow, J. Fluid Mech. **277**, 197 (1994).
[9] P. A. Elofsson, M. Kawakami, and P. H. Alfredsson, Experiments on the stability of streamwise streaks in plane Poiseuille flow, Phys. Fluids **11**, 915 (1999).
[10] P. A. Elofsson and P. H. Alfredsson, An experimental study of oblique transition in plane Poiseuille flow, J. Fluid Mech. **358**, 177 (1998).
[11] M. Acarlar and C. Smith, A study of hairpin vortices in a laminar boundary layer. Part 2. Hairpin vortices generated by fluid injection, J. Fluid Mech. **175**, 43 (1987).
[12] B. A. Singer and R. D. Joslin, Metamorphosis of a hairpin vortex into a young turbulent spot, Phys. Fluids **6**, 3724 (1994).
[13] R. G. Jacobs and D. S. Henningson, Evaluation of data from direct numerical simulations of transition due to freestream turbulence, Annual Research Briefs, Center for Turbulence Research-Stanford University, 1999, https://web.stanford.edu/group/ctr/ResBriefs99/henningson2.pdf.
[14] P. Alfredsson and M. Matsubara, Free-stream turbulence, streaky structures and transition in boundary layer flows, in *Fluids 2000 Conference and Exhibit* (AIAA, Reston, VA, 2000), p. 2534.
[15] S. Berlin, A. Lundbladh, and D. Henningson, Spatial simulations of oblique transition in a boundary layer, Phys. Fluids **6**, 1949 (1994).
[16] P. Schlatter, L. Brandt, H. De Lange, and D. S. Henningson, On streak breakdown in bypass transition, Phys. Fluids **20**, 101505 (2008).
[17] K. M. Butler and B. F. Farrell, Optimal perturbations and streak spacing in wall-bounded turbulent shear flow, Phys. Fluids A **5**, 774 (1993).
[18] S. Chernyshenko and M. Baig, Streaks and vortices in near-wall turbulence, Philos. Trans. R. Soc. A **363**, 1097 (2005).
[19] S. Chernyshenko and M. Baig, The mechanism of streak formation in near-wall turbulence, J. Fluid Mech. **544**, 99 (2005).
[20] J. C. Del Alamo and J. Jimenez, Linear energy amplification in turbulent channels, J. Fluid Mech. **559**, 205 (2006).
[21] G. Pujals, M. García-Villalba, C. Cossu, and S. Depardon, A note on optimal transient growth in turbulent channel flows, Phys. Fluids **21**, 015109 (2009).
[22] Y. Hwang and C. Cossu, Linear non-normal energy amplification of harmonic and stochastic forcing in the turbulent channel flow, J. Fluid Mech. **664**, 51 (2010).
[23] B. J. McKeon and A. S. Sharma, A critical-layer framework for turbulent pipe flow, J. Fluid Mech. **658**, 336 (2010).
[24] J. Kim and J. Lim, A linear process in wall-bounded turbulent shear flows, Phys. Fluids **12**, 1885 (2000).
[25] W. M. Orr, The stability or instability of the steady motions of a perfect liquid and of a viscous liquid. Part II: A viscous liquid, Proc. R. Ir. Acad. Sect. A **27**, 69 (1907).
[26] B. F. Farrell, Optimal excitation of perturbations in viscous shear flow, Phys. Fluids **31**, 2093 (1988).
[27] P. J. Schmid, D. S. Henningson, and D. Jankowski, Stability and transition in shear flows. Applied Mathematical Sciences, Vol. 142, Appl. Mech. Rev. **55**, B57 (2002).
[28] S. C. Reddy, P. J. Schmid, J. S. Baggett, and D. S. Henningson, On stability of streamwise streaks and transition thresholds in plane channel flows, J. Fluid Mech. **365**, 269 (1998).
[29] P. Andersson, L. Brandt, A. Bottaro, and D. S. Henningson, On the breakdown of boundary layer streaks, J. Fluid Mech. **428**, 29 (2001).
[30] J. Hœpffner, L. Brandt, and D. S. Henningson, Transient growth on boundary layer streaks, J. Fluid Mech. **537**, 91 (2005).
[31] W. Schoppa and F. Hussain, Coherent structure generation in near-wall turbulence, J. Fluid Mech. **453**, 57 (2002).
[32] C. Cossu, M. Chevalier, and D. S. Henningson, Optimal secondary energy growth in a plane channel flow, Phys. Fluids **19**, 058107 (2007).

[33] C. Cossu, L. Brandt, S. Bagheri, and D. S. Henningson, Secondary threshold amplitudes for sinuous streak breakdown, Phys. Fluids **23**, 074103 (2011).
[34] C. C. T. Pringle and R. R. Kerswell, Using Nonlinear Transient Growth to Construct the Minimal Seed for Shear Flow Turbulence, Phys. Rev. Lett. **105**, 154502 (2010).
[35] S. Cherubini, P. De Palma, J.-C. Robinet, and A. Bottaro, Rapid path to transition via nonlinear localized optimal perturbations in a boundary-layer flow, Phys. Rev. E **82**, 066302 (2010).
[36] C. C. Pringle, A. P. Willis, and R. R. Kerswell, Minimal seeds for shear flow turbulence: Using nonlinear transient growth to touch the edge of chaos, J. Fluid Mech. **702**, 415 (2012).
[37] S. M. E. Rabin, C. P. Caulfield, and R. R. Kerswell, Triggering turbulence efficiently in plane Couette flow, J. Fluid Mech. **712**, 244 (2012).
[38] Y. Duguet, A. Monokrousos, L. Brandt, and D. S. Henningson, Minimal transition thresholds in plane Couette flow, Phys. Fluids **25**, 084103 (2013).
[39] R. Kerswell, Nonlinear nonmodal stability theory, Annu. Rev. Fluid Mech. **50**, 319 (2018).
[40] J. D. Skufca, J. A. Yorke, and B. Eckhardt, Edge of Chaos in a Parallel Shear Flow, Phys. Rev. Lett. **96**, 174101 (2006).
[41] B. Eckhardt, T. M. Schneider, B. Hof, and J. Westerweel, Turbulence transition in pipe flow, Annu. Rev. Fluid Mech. **39**, 447 (2007).
[42] P. Schmid and D. Henningson, A new mechanism for rapid transition involving a pair of oblique waves, Phys. Fluids A **4**, 1986 (1992).
[43] Y. Duguet, L. Brandt, and B. R. J. Larsson, Towards minimal perturbations in transitional plane Couette flow, Phys. Rev. E **82**, 026316 (2010).
[44] L. Kelvin, Stability of fluid motion: Rectilinear motion of viscous fluid between two parallel plates, Philos. Mag. **24**, 188 (1887).
[45] H. Moffat, The interaction of turbulence with strong shear, in *Proceedings of the URSI-IUGG International Colloquium on Atmospheric Turbulence and Radio Wave Propagation, Moscow, June 1965*, edited by A. M. Yaglom and V. I. Tatarsky (Nauka, Moscow, 1967), p. 139.
[46] A. Craik and W. Criminale, Evolution of wavelike disturbances in shear flows: A class of exact solutions of the Navier-Stokes equations, Proc. R. Soc. London, Ser. A **406**, 13 (1986).
[47] B. F. Farrell and P. J. Ioannou, Optimal excitation of three-dimensional perturbations in viscous constant shear flow, Phys. Fluids A **5**, 1390 (1993).
[48] M. R. Jovanović and B. Bamieh, Componentwise energy amplification in channel flows, J. Fluid Mech. **534**, 145 (2005).
[49] J. A. Weideman and S. C. Reddy, A MATLAB differentiation matrix suite, ACM Trans. Math. Softw. **26**, 465 (2000).
[50] T. R. Bewley, *Numerical Renaissance: Simulation, Optimization, & Control* (Renaissance Press, San Diego, CA, 2012).
[51] Q. Yang, A. P. Willis, and Y. Hwang, Exact coherent states of attached eddies in channel flow, J. Fluid Mech. **862**, 1029 (2019).
[52] M. Nagata, Three-dimensional finite-amplitude solutions in plane Couette flow: Bifurcation from infinity, J. Fluid Mech. **217**, 519 (1990).
[53] J. M. Hamilton, J. Kim, and F. Waleffe, Regeneration mechanisms of near-wall turbulence structures, J. Fluid Mech. **287**, 317 (1995).
[54] J. Jiménez and P. Moin, The minimal flow unit in near-wall turbulence, J. Fluid Mech. **225**, 213 (1991).
[55] D. Barkley, Theoretical perspective on the route to turbulence in a pipe, J. Fluid Mech. **803**, P1 (2016).
[56] J. Moehlis, H. Faisst, and B. Eckhardt, A low-dimensional model for turbulent shear flows, New J. Phys. **6**, 56 (2004).
[57] B. Hof, J. Westerweel, T. M. Schneider, and B. Eckhardt, Finite lifetime of turbulence in shear flows, Nature (London) **443**, 59 (2006).
[58] B. Eckhardt, H. Faisst, A. Schmiegel, and T. M. Schneider, Dynamical systems and the transition to turbulence in linearly stable shear flows, Philos. Trans. R. Soc. A **366**, 1297 (2008).
[59] D. S. Park and P. Huerre, Primary and secondary instabilities of the asymptotic suction boundary layer on a curved plate, J. Fluid Mech. **283**, 249 (1995).

[60] A. Monokrousos, E. Åkervik, L. Brandt, and D. S. Henningson, Global three-dimensional optimal disturbances in the Blasius boundary-layer flow using time-steppers, J. Fluid Mech. **650**, 181 (2010).
[61] J. Jiménez, How linear is wall-bounded turbulence?, Phys. Fluids **25**, 110814 (2013).
[62] J. Jiménez, Direct detection of linearized bursts in turbulence, Phys. Fluids **27**, 065102 (2015).
[63] J. Encinar and J. Jiménez, Momentum transfer by linearised eddies in turbulent channel flows, J. Fluid Mech. **895**, A23 (2020).
[64] P. Doohan, A. P. Willis, and Y. Hwang, Minimal multi-scale dynamics of near-wall turbulence (to be published).
[65] O. Flores and J. Jiménez, Hierarchy of minimal flow units in the logarithmic layer, Phys. Fluids **22**, 071704 (2010).
[66] Y. Hwang and C. Cossu, Self-Sustained Process at Large Scales in Turbulent Channel Flow, Phys. Rev. Lett. **105**, 044505 (2010).
[67] Y. Hwang and Y. Bengana, Self-sustaining process of minimal attached eddies in turbulent channel flow, J. Fluid Mech. **795**, 708 (2016).